



1 Seamless mapping of long-term (2010-2020) daily global XCO₂ and 2 XCH₄ from GOSAT, OCO-2, and CAMS-EGG4 with a 3 spatiotemporally self-supervised fusion method

4 Yuan Wang¹, Qiangqiang Yuan^{1,2}, Tongwen Li³, Yuanjian Yang⁴, Siqin Zhou¹, Liangpei Zhang⁵

5 ¹School of Geodesy and Geomatics, Wuhan University, Wuhan, Hubei, 430079, China.

6 ²The Key Laboratory of Geospace Environment and Geodesy, Ministry of Education, Wuhan University, Wuhan, Hubei,
7 430079, China.

8 ³School of Geospatial Engineering and Science, Sun Yat-sen University, Guangzhou, Guangdong, 519082, China.

9 ⁴School of Atmospheric Physics, Nanjing University of Information Science & Technology, Nanjing, Jiangsu, 210044,
10 China.

11 ⁵The State Key Laboratory of Information Engineering in Surveying, Mapping and Remote Sensing, Wuhan University,
12 Wuhan, Hubei, 430079, China.

13 *Correspondence to:* Qiangqiang Yuan (qyuan@sgg.whu.edu.cn)

14 **Abstract.** Precise and continuous monitoring on long-term carbon dioxide (CO₂) and methane (CH₄) over the globe is of great
15 importance, which can help study global warming and achieve the goal of carbon neutrality. Nevertheless, the available
16 observations of CO₂ and CH₄ from satellites are generally sparse, and current fusion methods to reconstruct their long-term
17 values on a global scale are few. To address this problem, we propose a novel spatiotemporally self-supervised fusion method
18 to establish long-term daily seamless XCO₂ and XCH₄ products from 2010 to 2020 over the globe at grids of 0.25°. A total of
19 three datasets are applied in our study, including GOSAT, OCO-2, and CAMS-EGG4. Attributed to the significant sparsity of
20 data from GOSAT and OCO-2, the spatiotemporal Discrete Cosine Transform is considered for our fusion task. Validation
21 results show that the proposed method achieves a satisfactory accuracy, with the σ (R^2) of ~ 1.18 ppm (> 0.9) and 11.3 ppb
22 (0.9) for XCO₂ and XCH₄ against TCCON measurements, respectively. Overall, the performance of fused results distinctly
23 exceeds that of CAMS-EGG4, which is also superior or close to those of GOSAT and OCO-2. Especially, our fusion method
24 can effectively correct the large biases in CAMS-EGG4 due to the issues from assimilation data, such as the unadjusted
25 anthropogenic emission inventories for COVID-19 lockdowns in 2020. Moreover, the fused results present coincident spatial
26 patterns with GOSAT and OCO-2, which accurately display the long-term and seasonal changes of globally distributed XCO₂
27 and XCH₄. The daily global seamless gridded (0.25°) XCO₂ and XCH₄ from 2010 to 2020 can be freely accessed at
28 <http://doi.org/10.5281/zenodo.7388893> (Wang et al., 2022b).



29 **1 Introduction**

30 As the most abundant greenhouse gases (GHGs) due to human activities, atmospheric carbon dioxide (CO₂) and methane
31 (CH₄) play significant roles in climate change and directly contribute to global warming (Meinshausen et al., 2009; Montzka
32 et al., 2011; Solomon et al., 2010; Yoro and Daramola, 2020; Shine et al., 2005). For decades, the rising anthropogenic surface
33 emissions of CO₂ and CH₄ result in their long-term rapid uptrends (Choulga et al., 2021; Moran et al., 2022; Lin et al., 2021;
34 Petrescu et al., 2021), which have greatly affected the carbon cycle (Battin et al., 2009; Sjögersten et al., 2014) and ecosystem
35 balance (Liu and Greaver, 2009; Hotchkiss et al., 2015). According to measurements from the Global Greenhouse Gas
36 Reference Network (<https://gml.noaa.gov/ccgg/>), annual surface CO₂ and CH₄ mole fractions break 412 parts per million (ppm)
37 and 1878 parts per billion (ppb) in 2020, with growths of ~ 68 ppm and 222 ppb since 1985, respectively. To mitigate global
38 warming, the Paris Agreement (<https://unfccc.int/process-and-meetings/the-paris-agreement/>) has indicated that the increment
39 of temperature should not exceed 2 °C (preferably to 1.5 °C) by comparison with the pre-industrial level. This requires all
40 efforts from the whole society to reach the global peaking of GHGs surface emissions as early as possible, especially for CO₂
41 and CH₄, which eventually create a carbon-neutral world by mid-century. Therefore, it is an urgent need to precisely and
42 continuously monitor atmospheric CO₂ and CH₄ on a global scale.

43 To date, remote sensing observations have been extensively adopted in plenty of domains (Wang et al., 2021a, 2022c; Zhou et
44 al., 2022), which also emerged as regular techniques to acquire globe-scale atmospheric CO₂ and CH₄ spatial patterns (He et
45 al., 2022a; Buchwitz et al., 2015; Bergamaschi et al., 2013). For instance, the EnviSat can provide global column-mean dry-
46 air mole fraction of CO₂ (XCO₂) and CH₄ (XCH₄) at a coarse resolution of 30×60 km², with the payload of the Scanning
47 Imaging Absorption Spectrometer for Atmospheric Cartography (Burrows et al., 1995; Beirle et al., 2018). The Thermal and
48 Near-Infrared Sensor for carbon Observations - Fourier Transform Spectrometer onboard the Greenhouse Gases Observing
49 Satellite (GOSAT) (Hamazaki et al., 2005; Velasco et al., 2019) can produce ~ 10-km XCO₂ and XCH₄ over the globe based
50 on three spectral bands. The Orbiting Carbon Observatory 2/3 (OCO-2/3) (Crisp et al., 2017; Doughty et al., 2022) carries
51 three-channel grating spectrometers to generate globally covered XCO₂ at a much finer spatial resolution of 1.29×2.25 km².
52 The Carbon Dioxide Spectrometer named CarbonSpec onboard the TanSat (Liu et al., 2018) of China launched in 2016, which
53 can accurately map high-resolution (~ 2 km) global XCO₂ spatial distribution.

54 As for long-term observations of XCO₂ and XCH₄, the operational products from GOSAT and OCO-2 are widely applied in
55 carbon-related applications, such as the computation of carbon fluxes (Fraser et al., 2013; Wang et al., 2019), inferring carbon
56 sources and sinks (Deng et al., 2014; Houweling et al., 2015), quantifying CO₂ and CH₄ emissions (Turner et al., 2015;
57 Hakkarainen et al., 2016), and estimation of terrestrial net ecosystem exchange (Jiang et al., 2022). Nevertheless, large-scale
58 missing data consists in the XCO₂ and XCH₄ products from GOSAT and OCO-2, which is attributed to the narrow swath of
59 their observations (Crisp et al., 2017) and contamination of cloud and aerosol (Taylor et al., 2016). Seamless information of



60 XCO₂ and XCH₄ can help better understand the driving factors of long-term variations for CO₂ and CH₄ due to surface
61 emissions and atmospheric transport (Kenea et al., 2023; Liu et al., 2020). In addition, full-coverage XCO₂ and XCH₄ products
62 are more useful to analyze carbon source-sink dynamics (Reithmaier et al., 2021; Crosswell et al., 2017) and impacts on climate
63 changes caused by the elevated CO₂ and CH₄ (Chen et al., 2021; Le Quéré et al., 2019). Hence, it is significant and essential
64 to assure the spatiotemporal continuity of XCO₂ and XCH₄ products from GOSAT and OCO-2, which is conducive to achieving
65 the goal of carbon neutrality.

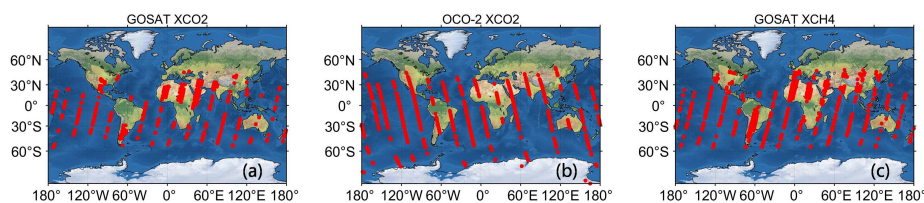
66 A lot of efforts have been made to generate seamless XCO₂ and XCH₄ products for GOSAT and OCO-2. Initially, interpolation-
67 based methods are widely utilized, such as the fixed rank kriging interpolation (Katzfuss and Cressie, 2011), semantic kriging
68 interpolation (Bhattacharjee et al., 2014), and space-time kriging interpolation (He et al., 2020; Li et al., 2022). However, the
69 interpolated results are usually performed at coarse spatial resolutions (e.g., 1°) and tend to show high uncertainties and over-
70 smoothed distribution due to the extreme sparsity of original data. At present, data fusion techniques (He et al., 2022a, b; Zhang
71 et al., 2022; Zhang and Liu, 2023; Siabi et al., 2019) have emerged as new methods to acquire full-coverage products for
72 GOSAT and OCO-2 at a high spatial resolution, which absorb advantages from multisource data. Generally, these methods
73 exploited machine learning algorithms to train an end-to-end fusion function with multiple seamless data (e.g., model and
74 reanalysis) as inputs. For example, Siabi et al. (2019) employed multi-layer perceptron and eight environmental variables (e.g.,
75 net primary productivity and leaf area index) to map full-coverage XCO₂ in Iran; He et al. (2022b) established seamless results
76 over China using the OCO-2 XCO₂ product, CarbonTracker model data, and auxiliary co-variates based on the light gradient
77 boosting machine; Zhang et al. (2022) proposed a geographically weighted neural network to produce full-coverage XCO₂
78 product across China by fusing the datasets from OCO-2, CAMS-EGG4 (reanalysis), and ERA5; and Zhang and Liu (2023)
79 adopted multiple datasets, e.g., EnviSat, GOSAT, OCO-2, CarbonTracker, and ERA5, and obtained long-term seamless XCO₂
80 product in China through a finely devised neural network.

81 These data fusion approaches provided high-quality results with seamless distribution and greatly enhance the data availability
82 for GOSAT and OCO-2. Nevertheless, the application areas of current fused products merely target at local or national scales,
83 which are insufficient for globe-scale researches. Meanwhile, existing data fusion frameworks are regarded as end-to-end
84 functions, which lack consideration for spatiotemporal self-correlation of original data (e.g., OCO-2). They normally require
85 massive auxiliary co-variates (e.g., ERA5) as inputs and consume a large time in training procedures. Moreover, only XCO₂
86 products are taken into account while the data fusion studies for XCH₄ products are scarce. In conclusion, it is valuable and
87 imperative to generate long-term globally distributed seamless XCO₂ and XCH₄ products for GOSAT and OCO-2 with an
88 efficient data fusion method, which considers the knowledge of their spatiotemporal self-correlation.

89 The present study focuses on generating long-term daily global seamless XCO₂ and XCH₄ products from 2010 to 2020 at the
90 grids of 0.25° via a spatiotemporally self-supervised fusion method. A total of three datasets are utilized in our study without



91 any auxiliary co-variables, including GOSAT, OCO-2, and CAMS-EGG4. CAMS-EGG4 can provide long-term gridded full-
92 coverage XCO₂ and XCH₄ datasets over the globe, which is suitable for our fusion task. Since the data from GOSAT and OCO-
93 2 is significantly sparse in space-time domain (see Fig. 1), the fusion procedures are difficult to be performed. By contrast,
94 frequency domain contains comprehensive information due to its more concentrated signal distribution. Discrete Cosine
95 Transform (DCT) (Rao and Yip, 2014) is an efficient algorithm to convert signal into frequency domain. In this study, a novel
96 self-supervised fusion method based on spatiotemporal DCT (S-STDCT) is developed for the fusion task. Details of the S-
97 STDCT fusion method are presented in Section 3. Validation results show that the S-STDCT fusion method achieves a
98 satisfactory performance. Generally, the accuracy of fused results largely exceeds that of CAMS-EGG4, which is also better
99 than or close to those of GSOAT and OCO-2.



100
101 **Figure 1.** An example of daily spatial footprints for (a) GOSAT XCO₂, (b) OCO-2 XCO₂, and (c) GOSAT XCH₄. Red points signify the
102 available data. Background maps are naturally shaded reliefs over the globe.

103 This paper arranges the remaining sections as follows. Section 2 describes the data records employed in our study, including
104 the XCO₂ and XCH₄ from in-situ stations, GOSAT, and CAMS-EGG4 and XCO₂ from OCO-2. Section 3 provides the
105 specification of the developed S-STDCT fusion method. Section 4 presents the experiment results, which consist of elaborative
106 validations against in-situ measurements and assessments of spatial distribution on multi-temporal scales. At last, conclusions
107 and future works are summarized in section 5.

108 2 Data description

109 2.1 GOSAT XCO₂ and XCH₄ products

110 A famous XCO₂ retrieval algorithm devised for GOSAT (Taylor et al., 2022), i.e., the Atmospheric CO₂ Observations from
111 Space (ACOS), employs three infrared spectral bands at ~ 0.76, 1.6, and 2.0 μm, which are denoted as Oxygen-A, CO₂ weak,
112 and CO₂ strong, respectively. Regarding XCH₄, the latest retrieval algorithm for GOSAT from the University of Leicester is
113 recently updated, which considers the ratio of XCH₄:XCO₂ as a proxy (Parker et al., 2020). It is based on the theory that the
114 impacts from atmospheric scattering and sensor are mostly similar for XCH₄ and XCO₂ in a shared absorption band at ~ 1.6
115 μm. The GOSAT XCO₂ and XCH₄ products are both performed at spatial resolutions of 10.5 km (diameter) over the globe
116 with revisit times of 3 days. In our study, the scientific data records of “XCO₂” in ACOS_L2_Lite_FP (level 2, bias-corrected,
117 V9r) and “XCH₄” in UoL-GHG-L2-CH4-GOSAT-OCPR (level 2, V9) are adopted. Furthermore, the QA records of “XCO₂



118 Quality Flag” and “XCH4 Quality Flag” are exploited to filter bad data. Relevant information of XCO₂ and XCH₄ products
 119 from GOSAT is shown in Table 1.
 120 **Table 1.** Detailed information of the datasets considered in this study.

Source	Scientific data record	Version	Spatial resolution	Temporal resolution	Period
GOSAT	XCO ₂	V9r	10.5 km (diameter)	Daily (~ 13:00 local time)	2010-2014
	XCO ₂ Quality Flag				
	XCH ₄	V9			2010-2020
OCO-2	XCH ₄ Quality Flag	V10r	1.29×2.25 km ²	Daily (~ 13:36 local time)	2015-2017
	XCO ₂				
	XCO ₂ Quality Flag	V11r			2018-2020
CAMS-EGG4	CO ₂ column-mean molar fraction	-	0.75°	3 hours	2010-2020
	CH ₄ column-mean molar fraction				

121 **2.2 OCO-2 XCO₂ product**

122 Apart from GOSAT, the ACOS XCO₂ retrieval algorithm is also applied to OCO-2 observations (Kiel et al., 2019), which
 123 utilizes the same bands of the Oxygen-A, CO₂ weak, and CO₂ strong. OCO-2 provides a global XCO₂ product at a high spatial
 124 resolution of 1.29×2.25 km² with a revisit time of 16 days. After 2015, the XCO₂ product from OCO-2 is used for fusion
 125 instead of GOSAT due to its more observation counts and better accuracy. In this study, the scientific data record of “XCO₂”
 126 in OCO2_L2_Lite_FP (level 2, bias-corrected) is applied in the fusion with CAMS-EGG4 using the developed method.
 127 Moreover, the quality assurance (QA) record of “XCO₂ Quality Flag” is adopted to filter bad data. Since the OCO-2 XCO₂
 128 product of the latest version (V11r) is still on processing, both data of V10r and V11r are considered in our study. Related
 129 information of XCO₂ product from OCO-2 is given in Table 1.

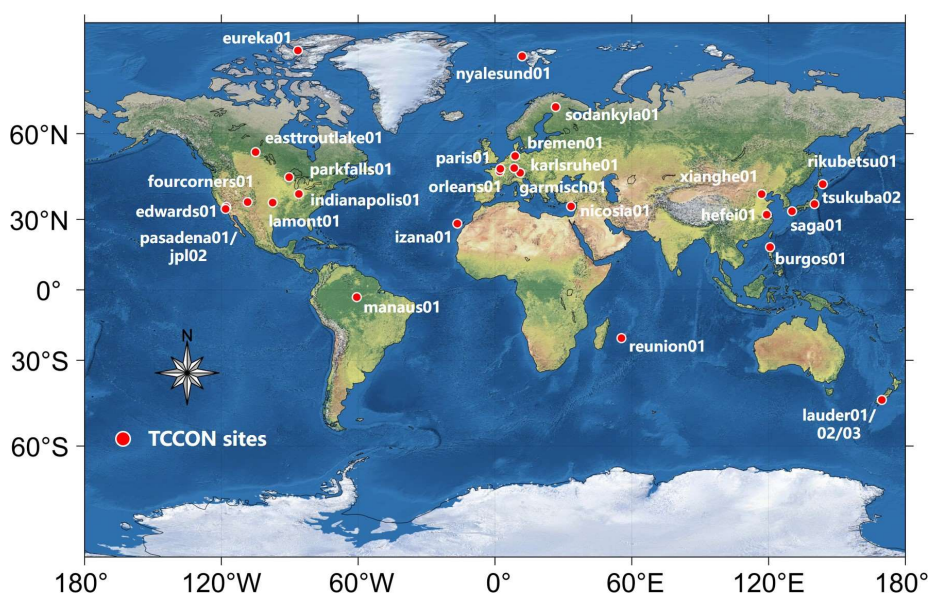
130 **2.3 CAMS-EGG4 GHGs reanalysis datasets**

131 CAMS-EGG4 is recent globally distributed operational GHGs reanalysis datasets supported by the European Centre for
 132 Medium-range Weather Forecasts (Agusti-Panareda et al., 2022). It assimilates the forecasts from the Integrated Forecasting
 133 System with multiple satellite products, which include Envisat, GOSAT, and Metop-A/B (August et al., 2012), via physical
 134 and chemistry principles. The CAMS-EGG4 can generate long-term gridded seamless XCO₂ and XCH₄ datasets and related
 135 fields at spatial and temporal resolutions of 0.75° and 3 hours, respectively. Unfortunately, there are a few limitations in CAMS-
 136 EGG4, such as the uncorrected anthropogenic emissions for CO₂ and CH₄ during COVID-19 lockdowns, which are
 137 scheduled to be fixed by the official team in the future (Agusti-Panareda et al., 2022). It is worth noting that the XCO₂ and
 138 XCH₄ products from GOSAT and OCO-2 employed in this paper are not assimilated in CAMS-EGG4. In our study, the
 139 scientific data records of “CO₂ column-mean molar fraction” and “CH₄ column-mean molar fraction” are exploited for the
 140 fusion with GOSAT and OCO-2 through the developed method. Details of CAMS-EGG4 datasets are provided in Table 1.



141 2.4 TCCON measurements

142 In our study, the XCO₂ and XCH₄ measurements provided by an international in-situ network, which is named after TCCON
143 (Wunch et al., 2011) (<https://tecondata.org/>), are utilized to validate the fused results. The in-situ measurements of TCCON
144 are extensively used in the validation for XCO₂ and XCH₄ products from GOSAT, OCO-2, and CAMS-EGG4 (Hong et al.,
145 2022; Yoshida et al., 2013; Wunch et al., 2017; Wu et al., 2018; Agusti-Panareda et al., 2022). Figure 2 depicts the spatial
146 locations of TCCON stations, with the marks of white-edged red circles. The measurements of version GGG2020 (Laughner
147 et al., 2022) from 29 stations around the world are adopted. Specific information of the stations is listed in Table 2.



148 **Figure 2.** Spatial locations of in-situ stations from TCCON used in the present study. The background map is a naturally shaded relief over
149 the globe.
150

151 3 Methodology

152 3.1 Data pre-processing

153 Data pre-processing is an important procedure to ensure the rationality and reliability of fused results. In this study, the values
154 of “QA=0” in XCO₂ and XCH₄ from GOSAT and OCO-2 are discarded, which filters the bad data. Besides, the CAMS-EGG4
155 XCO₂ and XCH₄ at a temporal resolution of 3 hours are averaged in a single day to produce daily datasets. Finally, the spatial
156 resolutions of XCO₂ and XCH₄ from GOSAT, OCO-2, and CAMS-EGG4 ought to be adjusted to the same value. A globally
157 covered grid of 721×1441 (0.25°) is employed in our study. The XCO₂ and XCH₄ from GOSAT, OCO-2, and CAMS-EGG4
158 are re-gridded to 0.25° using the area-weighted aggregation (Wang et al., 2021b) and Inverse Distance Weighted (Mueller et
159 al., 2004) interpolation, respectively.



160 **Table 2.** Detailed information of TCCON in-situ stations adopted in our study. No.: number.

No.	Site name	Latitude	Longitude	Location	Start date	End date
1	bremen01	53.10	8.85	Europe	2010-01-01	2020-12-31
2	burgos01	18.53	120.65	Asia	2017-03-03	2020-04-30
3	easttroutlake01	54.36	-104.99	North America	2016-10-03	2020-12-31
4	edwards01	34.96	-117.88	North America	2013-07-20	2020-12-31
5	eureka01	80.05	-86.42	North America	2010-07-24	2020-07-07
6	fourcorners01	36.80	-108.48	North America	2013-03-16	2013-10-03
7	garmisch01	47.48	11.06	Europe	2010-01-01	2020-12-31
8	hefei01	31.90	119.17	Asia	2016-01-08	2020-12-31
9	indianapolis01	39.86	-86.00	North America	2012-08-23	2012-12-01
10	izana01	28.31	-16.50	Atlantic Ocean	2014-01-02	2020-12-31
11	jp102	34.20	-118.18	North America	2011-05-19	2018-05-14
12	karlsruhe01	49.10	8.44	Europe	2014-01-15	2020-12-31
13	lauder01	36.60	-97.49	Oceania	2010-01-01	2010-02-19
14	lauder02	-45.04	169.68	Oceania	2013-01-02	2018-09-30
15	lauder03	-45.04	169.68	Oceania	2018-10-02	2020-12-31
16	lamont01	-45.04	169.68	North America	2010-01-01	2020-12-31
17	manaus01	-3.21	-60.60	South America	2014-09-30	2015-07-27
18	nicosia01	35.14	33.38	Asia	2019-09-03	2020-12-31
19	nyalesund01	78.92	11.92	Arctic Ocean	2010-01-01	2020-12-31
20	orleans01	47.96	2.11	Europe	2010-01-01	2020-12-31
21	paris01	48.85	2.36	Europe	2014-09-23	2020-12-31
22	parkfalls01	45.94	-90.27	North America	2010-01-01	2020-12-31
23	pasadena01	34.14	-118.13	North America	2012-09-20	2020-12-31
24	reunion01	-20.90	55.48	Indian Ocean	2015-03-01	2020-07-18
25	rikubetsu01	43.46	143.77	Asia	2014-06-24	2020-12-31
26	saga01	33.24	130.29	Asia	2011-07-28	2020-12-31
27	sodankyla01	67.37	26.63	Europe	2018-03-05	2020-12-31
28	tsukuba02	36.05	140.12	Asia	2014-03-28	2020-12-31
29	xianghe01	39.80	116.96	Asia	2018-06-14	2020-12-31

161 **3.2 Spatiotemporally self-supervised fusion method**

162 Since the sparsity of data from GOSAT and OCO-2 is significant in space-time domain (see Fig. 1), it is difficult to perform
 163 fusion procedures for them. In contrast, frequency domain is more suitable because of its concentrated signal distribution. DCT
 164 is an efficient algorithm to transform signal into frequency domain (Rao and Yip, 2014), which has been widely applied in
 165 image compression (Cintra and Bayer, 2011), geophysical data filtering (El-Mahallawy and Hashim, 2013), and remote sensing
 166 data reconstruction (Wang et al., 2012, 2022a; Fredj et al., 2016; Pham et al., 2019). In our study, a novel self-supervised fusion
 167 method based on spatiotemporal DCT, i.e., S-STDCT, is developed for the fusion task, which fully adopts the spatiotemporal
 168 knowledge of self-correlation in GOSAT and OCO-2 products.

169 **3.2.1 Spatiotemporal DCT**

170 A total of eight types of DCT are proposed, among which the second type (type-II) is commonly utilized due to its simple
 171 calculation and broad application range (Rao and Yip, 2014). Hence, the type-II DCT is considered in this study. The
 172 spatiotemporal DCT is a 3-dimensional form (hereafter *STDCT*), which can be expressed as Eq. (1):



$$173 \quad X(u, v, w) = c(u)c(v)c(w) \sum_{i=0}^{M-1} \sum_{j=0}^{N-1} \sum_{t=0}^{P-1} x(i, j, t) \cos \left[\frac{(i+0.5)\pi}{M} u \right] \cos \left[\frac{(j+0.5)\pi}{N} v \right] \cos \left[\frac{(t+0.5)\pi}{P} w \right], \quad (1)$$

$$174 \quad \text{where } c(u) = \begin{cases} \sqrt{\frac{1}{M}}, u = 0 \\ \sqrt{\frac{2}{M}}, u \neq 0 \end{cases}, \quad c(v) = \begin{cases} \sqrt{\frac{1}{N}}, v = 0 \\ \sqrt{\frac{2}{N}}, v \neq 0 \end{cases}, \quad c(w) = \begin{cases} \sqrt{\frac{1}{P}}, w = 0 \\ \sqrt{\frac{2}{P}}, w \neq 0 \end{cases}; \quad x \text{ indicates the original 3-dimensional tensor; } i, j,$$

175 and t represent the row, column, and temporal sequence, respectively ($i \in [0, M-1]$, $j \in [0, N-1]$, and $t \in [0, P-1]$); X
 176 signifies the transformed 3-dimensional tensor; u , v , and w denote the transformed coordinates in frequency domain, which
 177 share the same ranges with i , j , and t (e.g., $u \in [0, M-1]$), respectively. The inverse transformation of *STDCT* (hereafter
 178 *ISTDCT*) is provided in Eq. (2):

$$179 \quad x(i, j, t) = c(u)c(v)c(w) \sum_{u=0}^{M-1} \sum_{v=0}^{N-1} \sum_{w=0}^{P-1} X(u, v, w) \cos \left[\frac{(i+0.5)\pi}{M} u \right] \cos \left[\frac{(j+0.5)\pi}{N} v \right] \cos \left[\frac{(t+0.5)\pi}{P} w \right], \quad (2)$$

180 3.2.2 Self-supervised fusion scheme with spatiotemporal knowledge

181 It has been documented that the XCO_2 and XCH_4 products derived from remote sensing satellites generally present better
 182 accuracy compared to reanalysis datasets (Agusti-Panareda et al., 2022; He et al., 2022a; Parker et al., 2020). Therefore, the
 183 brand new XCO_2 and XCH_4 products from GOSAT and OCO-2 are regarded as the criteria (or ground truths), which will be
 184 fused with CAMS-EGG4 datasets. At first, a spatially and temporally varying function relationship (see Eq. (3)) is
 185 hypothesized between GOSAT/OCO-2 and CAMS-EGG4 XCO_2/XCH_4 values.

$$186 \quad XG_s = f(XG_c, Row, Col, Time), \quad (3)$$

187 where XG_s denotes the XCO_2/XCH_4 values from GOSAT/OCO-2; XG_c indicates the XCO_2/XCH_4 values from CAMS-EGG4;
 188 Row , Col , and $Time$ represent the row (or latitude), column (or longitude), and temporal sequence, respectively. To conveniently
 189 solve this problem, Eq. (3) is simplified into the scalar product form of XG_c and a spatially and temporally varying tensor
 190 (defined as δ), as shown in Eq. (4):

$$191 \quad XG_s = XG_c * \delta(Row, Col, Time), \quad (4)$$

192 Afterward, the factor (i.e., δ) can be acquired using the XCO_2/XCH_4 values at the grids where the GOSAT/OCO-2 and CAMS-
 193 EGG4 data are both available. In our study, a self-supervised fusion scheme is introduced to solve Eq. (4) based on the
 194 spatiotemporal knowledge of self-correlation in GOSAT and OCO-2 products. Due to the large sparsity of data from GOSAT
 195 and OCO-2 in space-time domain, the *STDCT* is applied for the fusion task.

196 Inspired by previous studies adopting the *STDCT* (Garcia, 2010; Wang et al., 2012, 2022a; Fredj et al., 2016; Pham et al.,
 197 2019), the S-*STDCT* fusion method searches for the spatially and temporally varying tensor, i.e., $\hat{\delta}$, that minimizes Eq. (5),
 198 including a residual (left) and a smoothing (right) term.

$$199 \quad E(\hat{\delta}) = \left\| \varphi^{\frac{1}{2}} * (\hat{\delta} - \delta) \right\|^2 + \varepsilon \|\nabla^2 \hat{\delta}\|^2, \quad (5)$$



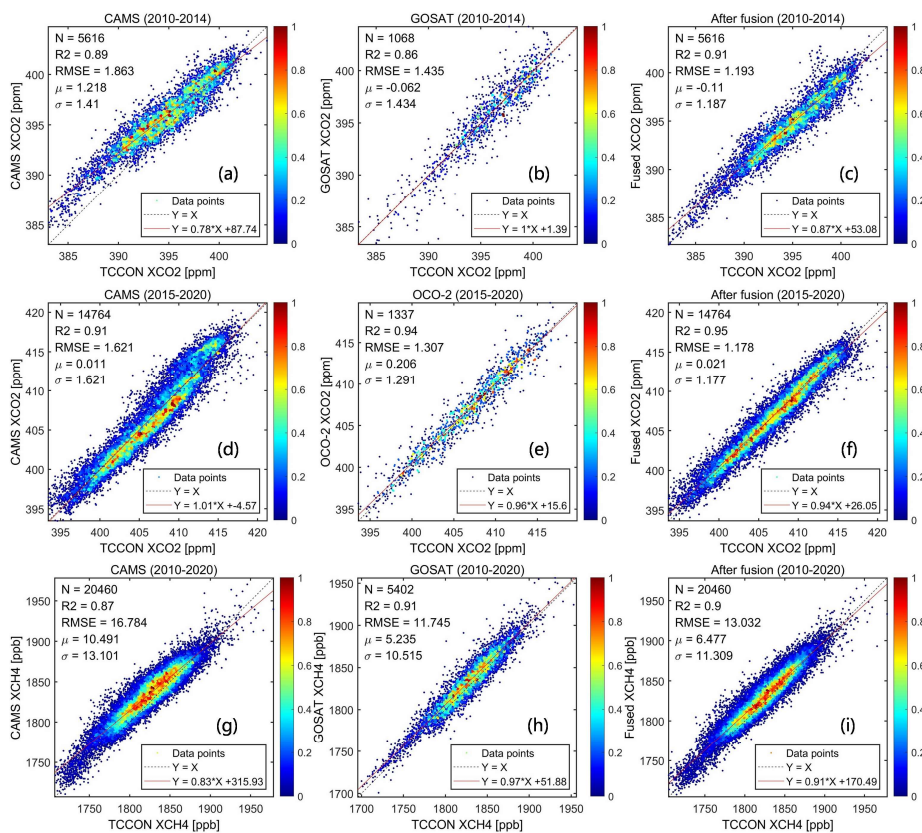
200 where $\| \cdot \|$ signifies the Euclidean norm; φ represents the binary mask showing the data is whether available or not; ε and
 201 ∇^2 indicate a smoothing factor and the Laplace operator, respectively. This equation can be solved by iterations via Eq. (6):

$$202 \quad \delta = \gamma \text{STDCT}(\rho * \text{STDCT}(\varphi * (\delta - \delta) + \delta)) + (1 - \gamma)\delta, \quad (6)$$

203 where γ is a relaxation factor to accelerate convergence; ρ indicates a 3-dimensional filter related to the smoothing term,
 204 which is defined in Eq. (7):

$$205 \quad \rho(d_1, d_2, d_3) = \frac{1}{1 + \varepsilon \sum_{k=1}^3 2 \left[1 - \cos \frac{(d_k - 1)\pi}{n_k} \right]}, \quad (7)$$

206 Here, d_k represents the d^{th} value along the k^{th} dimension ($k = 1, 2,$ and 3); n_k denotes the size of δ along the k^{th} dimension.
 207 Namely, $d_1, d_2,$ and d_3 stand for $u, v,$ and w (see Eq. (1)), respectively. In this study, the number of total iterations, $\gamma,$ and
 208 ε are empirically configured to 100, 1.5, and a range from 10^3 to 10^{-1} (spaced with 100 intervals), respectively. It is worth
 209 noting that δ is initialized through the temporal nearest neighbor interpolation. Regarding the grids where the data is missing
 210 during the whole temporal sequence, δ is initially set to 1. More details about the solution steps can be found in Garcia (2010).

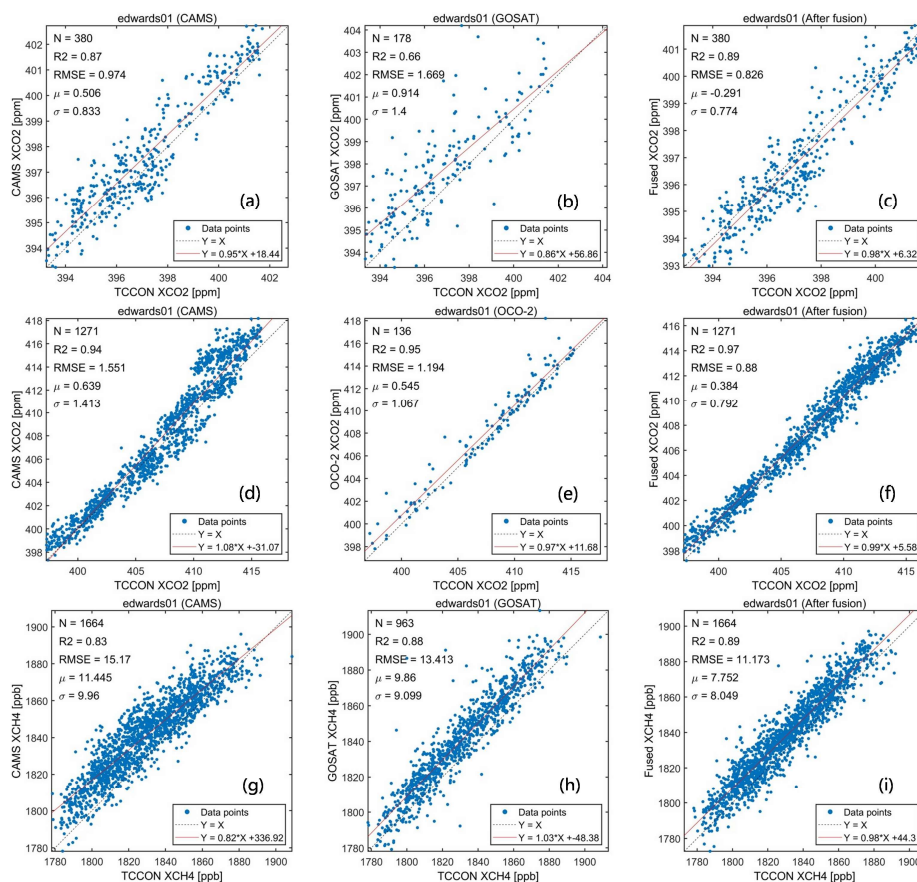


211
 212 **Figure 3.** Density scatter-plots of the in-situ validation results for (a, d, and g) CAMS-EGG4, (b and h) GOSAT, (e) OCO-2, and (c, f, and
 213 i) fused results. Black dotted and red full lines stand for the 1:1 and fitted lines, respectively. Color ramps show the normalized densities of
 214 data points. X: TCCON data; Y: CAMS-EGG4/GOSAT/OCO-2/fused data. Unit: ppm/ppb to $\text{XCO}_2/\text{XCH}_4$ for RMSE, $\mu,$ and σ .



215 3.3 Evaluation schemes

216 In our study, the evaluation schemes include in-situ validations and assessments of spatial distribution. To be specific, the
 217 GOSAT, OCO-2, CAMS-EGG4, and fused XCO₂ and XCH₄ are validated against TCCON measurements, which consists of
 218 the comparisons for overall and individual in-situ stations. The spatial distribution of the GOSAT, OCO-2, CAMS-EGG4, and
 219 fused XCO₂ and XCH₄ are assessed on multi-temporal scales, i.e., multi-year mean, seasonal, and annual. A total of four metrics
 220 are exploited, covering the Determination-Coefficient (R²), Root-Mean-Square-Error (RMSE), Mean-Bias (μ), and Standard-
 221 Deviation of Bias (σ). The significance levels of p < 0.01 are applied in the computations of all metrics.



222
 223 **Figure 4.** Scatter-plots of the in-situ validation results for (a, d, and g) CAMS-EGG4, (b and h) GOSAT, (e) OCO-2, and (c, f, and i) fused
 224 results on edwards01. Black dotted and red full lines stand for the 1:1 and fitted lines, respectively. X: TCCON data; Y: CAMS-
 225 EGG4/GOSAT/OCO-2/fused data. Unit: ppm/ppb to XCO₂/XCH₄ for RMSE, μ, and σ.

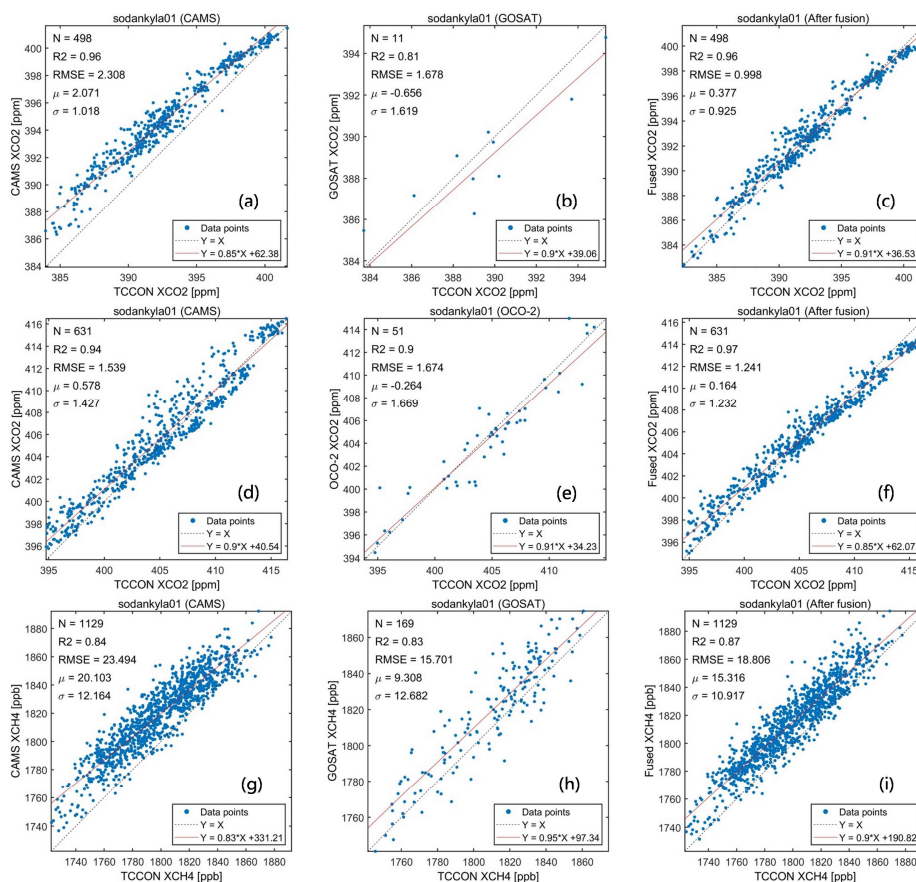
226 4 Experiment results and discussions

227 4.1 Overall in-situ validation

228 As displayed in Fig. 2, the XCO₂ and XCH₄ measurements from 29 TCCON in-situ stations are adopted for the validation,
 229 which evenly distribute over the globe. In this study, TCCON measurements of ± 1 hour on the satellite overpass times (~



230 13:00 and 13:36 local time, see Table 2) are co-matched with the CAMS-EGG4/GOSAT/OCO-2/fused data around each station
 231 with a diameter of 2°. Figure 3 depicts the overall in-situ validation results for the CAMS-EGG4, GOSAT, OCO-2, and fused
 232 results. The amounts of data points (N) are sufficient (e.g., 1337 for OCO-2 XCO₂ and 5402 for GOSAT XCH₄) to support the
 233 reliability of validation results.



234
 235 **Figure 5.** Scatter-plots of the in-situ validation results for (a, d, and g) CAMS-EGG4, (b and h) GOSAT, (e) OCO-2, and (c, f, and i) fused
 236 results on sodankyla01. Black dotted and red full lines stand for the 1:1 and fitted lines, respectively. X: TCCON data; Y: CAMS-
 237 EGG4/GOSAT/OCO-2/fused data. Unit: ppm/ppb to XCO₂/XCH₄ for RMSE, μ , and σ .

238 As shown in Fig. 3, the XCO₂ from OCO-2 and XCH₄ from GOSAT perform better than those from CAMS-EGG4, with larger
 239 R², smaller RMSE, and smaller σ . After fusion, the XCO₂ (2015-2020) and XCH₄ (2010-2020) present a greatly superior
 240 accuracy compared to CAMS-EGG4, of which the RMSE (σ) improvements are 0.443 (0.444) ppm and 3.752 (1.792) ppb for
 241 XCO₂ and XCH₄, respectively. Meanwhile, the accuracy of the fused results is higher than and close to those of OCO-2 XCO₂
 242 and GOSAT XCH₄, respectively. These suggest that the proposed fusion method achieves a satisfactory result. Furthermore,
 243 the performance of XCO₂ from GOSAT is similar to that of CAMS-EGG4. However, the fused XCO₂ (2010-2014) shows
 244 higher accuracy by comparison with both CAMS-EGG4 and GOSAT, indicating the spatiotemporally local fusion ability of S-
 245 STDCT. In conclusion, our fusion method can successfully fuse the data from CAMS-EGG4 and satellites, which effectively



246 generates GOSAT-like and OCO-2-like values.

247 **Table 3.** Metrics of the individual in-situ validation results for CAMS-EGG4, GOSAT, and fused XCO₂. The best and second metrics are
 248 denoted with bold and underlined fonts. CE: CAMS-EGG4; AF: after fusion. Unit: ppm for RMSE and σ .

Site name	R ²			RMSE			σ		
	CE	GOSAT	AF	CE	GOSAT	AF	CE	GOSAT	AF
bremen01	<u>0.91</u>	0.85	0.92	2.810	<u>1.732</u>	1.533	<u>1.376</u>	1.757	1.189
edwards01	<u>0.87</u>	0.66	0.89	<u>0.974</u>	1.669	0.826	<u>0.833</u>	1.400	0.774
fourcorners01	<u>0.88</u>	0.91	0.86	1.237	<u>0.867</u>	0.844	0.848	0.590	<u>0.801</u>
garmisch01	<u>0.91</u>	0.86	0.93	2.141	<u>1.575</u>	1.070	<u>1.275</u>	1.592	1.067
jpl02	<u>0.89</u>	0.86	0.90	1.535	<u>1.299</u>	1.075	<u>0.961</u>	1.299	0.918
saga01	0.90	<u>0.91</u>	0.93	<u>1.362</u>	1.494	1.333	1.313	<u>1.201</u>	1.065
lauder02	<u>0.83</u>	0.70	0.87	0.584	1.095	<u>0.606</u>	0.585	1.088	<u>0.600</u>
lamont01	<u>0.79</u>	0.88	0.88	1.928	<u>0.986</u>	0.976	1.327	0.973	<u>0.976</u>
orleans01	<u>0.89</u>	0.75	0.91	2.105	<u>1.666</u>	0.964	<u>1.144</u>	1.440	0.964
parkfalls01	<u>0.92</u>	0.86	0.93	2.088	<u>1.703</u>	1.138	<u>1.309</u>	1.697	1.137
pasadena01	0.70	<u>0.74</u>	0.75	1.260	<u>1.296</u>	1.642	<u>1.261</u>	1.287	1.177
sodankyla01	0.96	<u>0.81</u>	0.96	2.308	<u>1.678</u>	0.998	<u>1.018</u>	1.619	0.925
tsukuba02	<u>0.80</u>	0.82	0.78	1.179	1.651	<u>1.494</u>	1.157	1.263	<u>1.202</u>

249 **Table 4.** Metrics of the individual in-situ validation results for CAMS-EGG4, OCO-2, and fused XCO₂. The best and second metrics are
 250 denoted with bold and underlined fonts. CE: CAMS-EGG4; AF: after fusion. Unit: ppm for RMSE and σ .

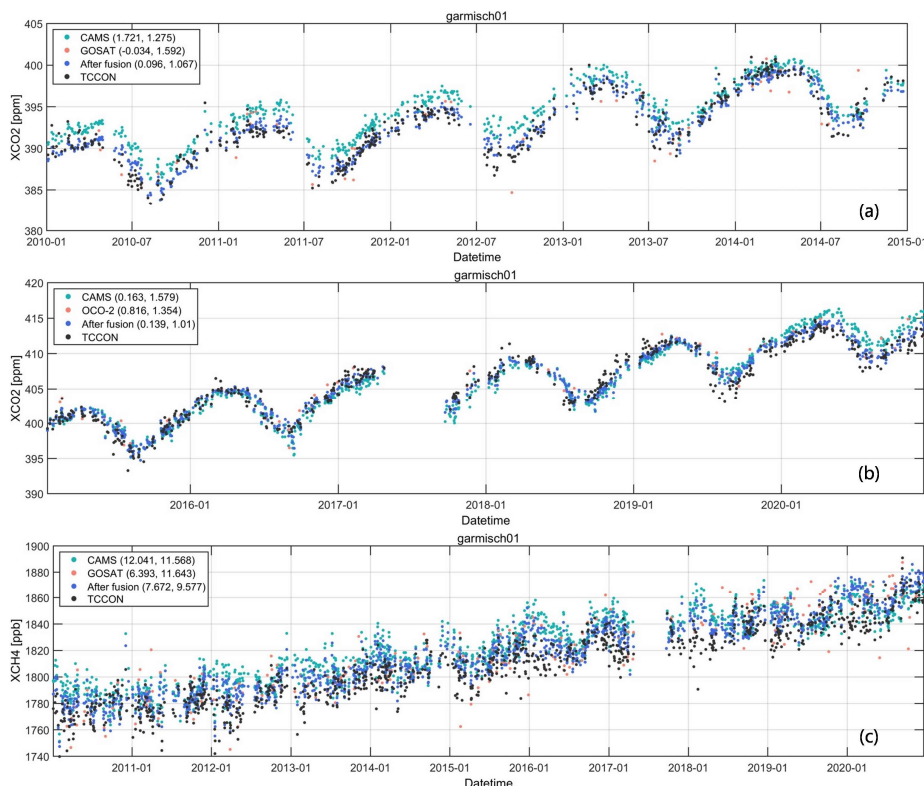
Site name	R ²			RMSE			σ		
	CE	OCO-2	AF	CE	OCO-2	AF	CE	OCO-2	AF
bremen01	0.91	0.99	<u>0.93</u>	1.718	1.126	<u>1.476</u>	1.678	1.066	<u>1.459</u>
burgos01	0.91	0.95	<u>0.94</u>	1.324	0.715	<u>0.933</u>	1.144	0.709	<u>0.823</u>
edwards01	0.94	<u>0.95</u>	0.97	1.551	<u>1.194</u>	0.880	1.413	<u>1.067</u>	0.792
easttroutlake01	<u>0.92</u>	0.87	0.94	<u>1.334</u>	1.802	1.195	<u>1.303</u>	1.812	1.196
eureka01	<u>0.94</u>	0.93	0.97	<u>2.081</u>	2.224	1.427	<u>1.436</u>	1.555	1.171
garmisch01	0.91	<u>0.93</u>	0.96	1.586	<u>1.569</u>	1.019	1.579	<u>1.354</u>	1.010
hefei01	0.88	0.97	<u>0.91</u>	1.447	1.163	<u>1.283</u>	1.450	0.735	<u>1.192</u>
izana01	<u>0.96</u>	0.88	0.99	<u>1.215</u>	1.413	0.576	<u>1.209</u>	1.417	0.555
jpl02	0.75	0.89	<u>0.76</u>	2.151	1.146	<u>1.525</u>	1.221	0.885	<u>1.174</u>
saga01	0.89	0.95	<u>0.94</u>	1.890	1.087	<u>1.263</u>	1.873	1.090	<u>1.254</u>
karlsruhe01	<u>0.89</u>	0.93	0.93	1.747	1.327	<u>1.375</u>	1.749	1.318	<u>1.376</u>
lauder02	<u>0.96</u>	0.89	0.97	1.213	<u>1.000</u>	0.492	<u>0.518</u>	0.993	0.469
lauder03	0.94	<u>0.72</u>	0.94	1.288	<u>1.064</u>	0.565	<u>0.863</u>	1.070	0.538
nicosia01	0.79	<u>0.91</u>	0.94	2.319	0.731	<u>0.862</u>	1.133	<u>0.661</u>	0.641
nyalesund01	<u>0.94</u>	0.93	0.97	<u>1.942</u>	2.233	1.664	<u>1.573</u>	1.707	1.446
lamont01	0.92	0.97	<u>0.96</u>	1.505	0.956	<u>0.964</u>	1.489	0.794	<u>0.929</u>
orleans01	0.92	<u>0.93</u>	0.96	1.450	<u>1.144</u>	1.108	1.361	<u>1.121</u>	1.007
parkfalls01	0.93	0.96	<u>0.95</u>	1.518	<u>1.210</u>	1.160	1.518	<u>1.211</u>	1.160
pasadena01	0.91	<u>0.93</u>	0.95	1.689	<u>1.543</u>	1.382	1.581	<u>1.329</u>	1.160
paris01	0.89	<u>0.92</u>	0.93	1.910	1.418	<u>1.451</u>	1.867	1.433	<u>1.437</u>
reunion01	<u>0.96</u>	0.97	0.97	1.276	<u>0.878</u>	0.874	<u>0.827</u>	0.886	0.812
rikubetsu01	0.90	0.96	<u>0.93</u>	1.688	1.023	<u>1.320</u>	1.667	1.033	<u>1.293</u>
sodankyla01	<u>0.94</u>	0.90	0.97	<u>1.539</u>	1.674	1.241	<u>1.427</u>	1.669	1.232
tsukuba02	0.92	0.94	<u>0.93</u>	1.429	1.169	<u>1.276</u>	1.322	1.134	<u>1.265</u>
xianghe01	0.61	0.89	<u>0.73</u>	2.513	1.411	<u>1.960</u>	2.487	1.430	<u>1.959</u>

251



252 **Table 5.** Metrics of the individual in-situ validation results for CAMS-EGG4, GOSAT, and fused XCH₄. The best and second metrics are
 253 denoted with bold and underlined fonts. CE: CAMS-EGG4; AF: after fusion. Unit: ppb for RMSE and σ .

Site name	R ²			RMSE			σ		
	CE	GOSAT	AF	CE	GOSAT	AF	CE	GOSAT	AF
bremen01	0.84	0.90	<u>0.87</u>	19.397	<u>15.328</u>	14.969	12.507	9.868	<u>10.938</u>
burgos01	<u>0.80</u>	0.89	0.89	10.981	<u>10.455</u>	8.096	9.194	6.136	<u>7.216</u>
edwards01	0.83	<u>0.88</u>	0.89	15.170	<u>13.413</u>	11.173	9.960	<u>9.099</u>	8.049
fourcorners01	0.40	0.71	<u>0.51</u>	14.732	7.714	<u>9.847</u>	9.711	6.710	<u>8.777</u>
garmisch01	0.83	<u>0.85</u>	0.89	16.693	<u>13.258</u>	12.267	<u>11.568</u>	11.643	9.577
hefei01	0.54	<u>0.56</u>	0.66	22.072	15.377	<u>16.814</u>	16.165	13.370	<u>13.826</u>
jpl02	0.81	0.88	<u>0.86</u>	16.989	9.679	<u>9.788</u>	11.288	8.840	<u>9.604</u>
saga01	0.85	0.92	<u>0.89</u>	11.299	9.089	<u>9.311</u>	10.091	8.422	<u>9.147</u>
karlsruhe01	0.70	<u>0.80</u>	0.81	13.688	<u>11.913</u>	10.042	11.564	<u>11.370</u>	9.177
lauder02	<u>0.66</u>	0.84	0.65	18.460	8.632	<u>11.323</u>	11.390	6.923	<u>10.189</u>
lauder03	0.46	0.76	<u>0.57</u>	16.568	8.531	<u>12.166</u>	10.965	6.491	<u>9.347</u>
lamont01	0.82	0.94	<u>0.88</u>	<u>11.762</u>	12.204	9.497	11.494	7.015	<u>9.460</u>
orleans01	<u>0.80</u>	0.88	0.88	18.341	<u>13.734</u>	13.305	12.038	<u>9.690</u>	9.395
parkfalls01	0.79	0.87	<u>0.84</u>	17.107	<u>14.892</u>	13.784	13.396	10.548	<u>11.519</u>
pasadena01	0.82	0.90	<u>0.88</u>	12.658	8.396	<u>8.845</u>	10.544	8.094	<u>8.802</u>
paris01	<u>0.75</u>	0.73	0.84	<u>12.313</u>	13.077	9.578	<u>10.319</u>	11.437	8.383
reunion01	<u>0.51</u>	0.41	0.73	18.245	<u>13.846</u>	10.092	<u>10.221</u>	11.427	7.432
rikubetsu01	0.60	0.81	<u>0.72</u>	21.166	<u>20.160</u>	18.250	15.263	11.481	<u>12.759</u>
sodankyla01	<u>0.84</u>	0.83	0.87	23.494	15.701	<u>18.806</u>	<u>12.164</u>	12.682	10.917
tsukuba02	0.77	0.86	<u>0.83</u>	11.726	8.165	<u>8.704</u>	9.401	7.623	<u>8.424</u>
xianghe01	<u>0.63</u>	0.69	<u>0.63</u>	14.851	15.840	<u>15.266</u>	<u>14.734</u>	13.752	14.736

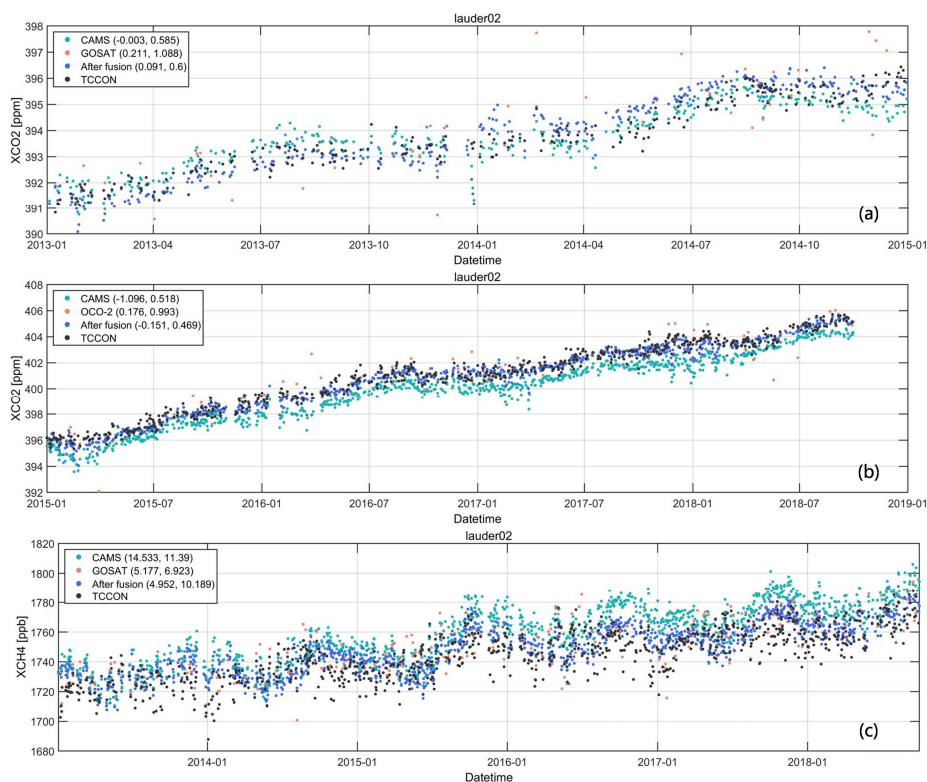


254
 255 **Figure 6.** Scatter-plots of the time series for daily CAMS-EGG4, GOSAT, OCO-2, fused, and TCCON data on garmisch01. The first and
 256 second numbers in the bracket represent μ and σ , respectively. Unit: ppm/ppb to XCO₂/XCH₄ for μ and σ .

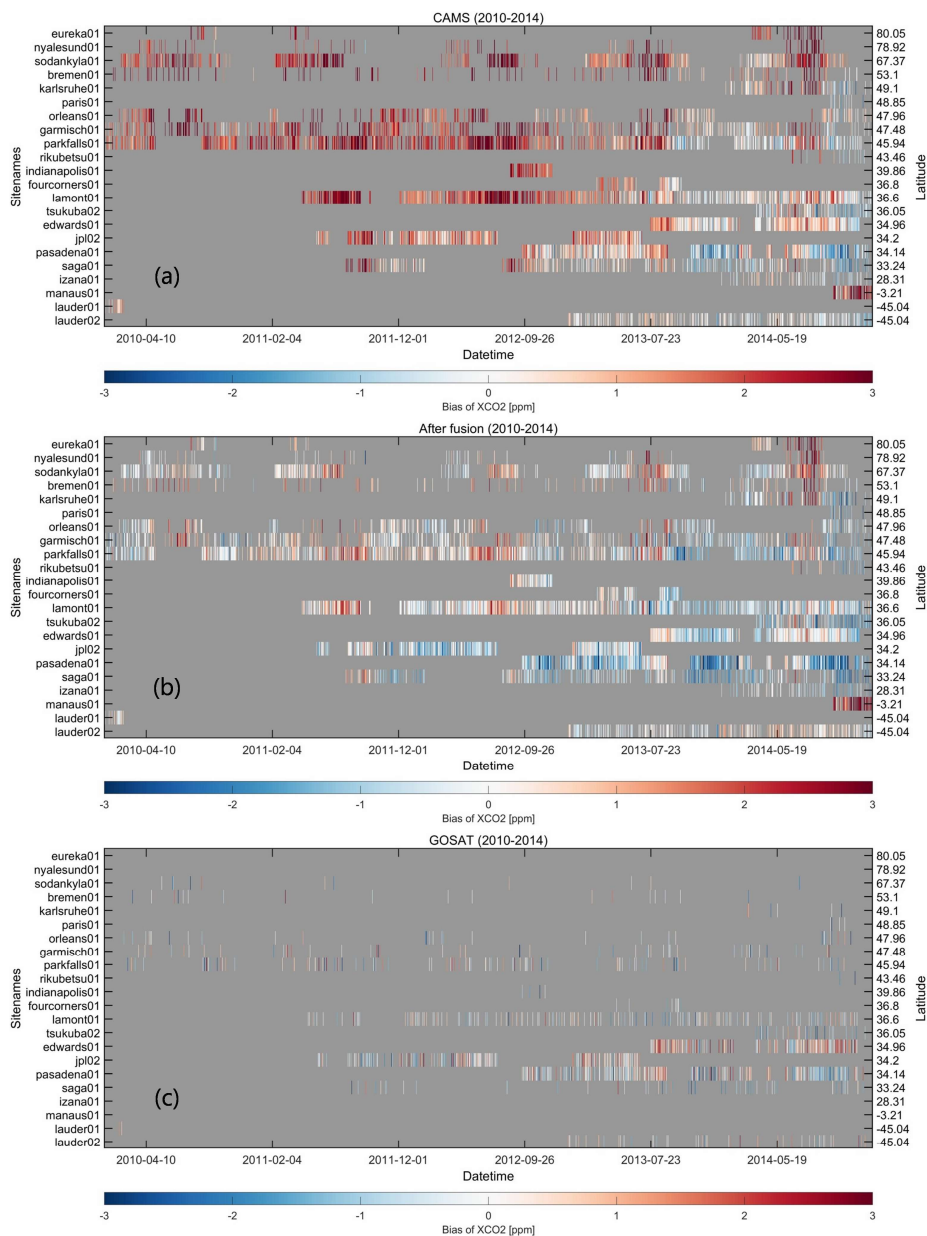


257 4.2 Individual in-situ validation and time series

258 Figure 4, 5, and S1-S24 illustrate the individual in-situ validation results for the CAMS-EGG4, GOSAT, OCO-2, and fused
259 results on each TCCON in-situ station. It is worth noting that only the stations where the individual validation results are
260 significant (p -level < 0.01) for all datasets (i.e., CAMS-EGG4, GOSAT, OCO-2, and the fused results) are presented. Since
261 the space of text is limited, two stations named edwards01 and sodankyla01 are selected as examples (see Fig. 4 and 5), which
262 locate in North America and Europe, respectively. As can be seen, the fused results achieve the best performance compared to
263 CAMS-EGG4, GOSAT, and OCO-2 on edwards01 and sodankyla01, with the R^2 ranging from 0.87 to 0.97. Especially, the
264 large overestimation of XCO_2 for CAMS-EGG4 on sodankyla01 ($\mu = 2.071$ ppm) is well mitigated after fusion ($\mu = 0.377$
265 ppm), even for the poor data availability of GOSAT ($N = 11$). This indicates the strong universality of the proposed fusion
266 method. The valid individual validation results on all stations are given in Table 3-5 (more details in the Supplement, Fig. S1-
267 S24). It can be observed that the performance of the fused results exceeds those of CAMS-EGG4 and GOSAT/OCO-2 for
268 almost all stations and $\sim 70\%$ of stations, respectively.

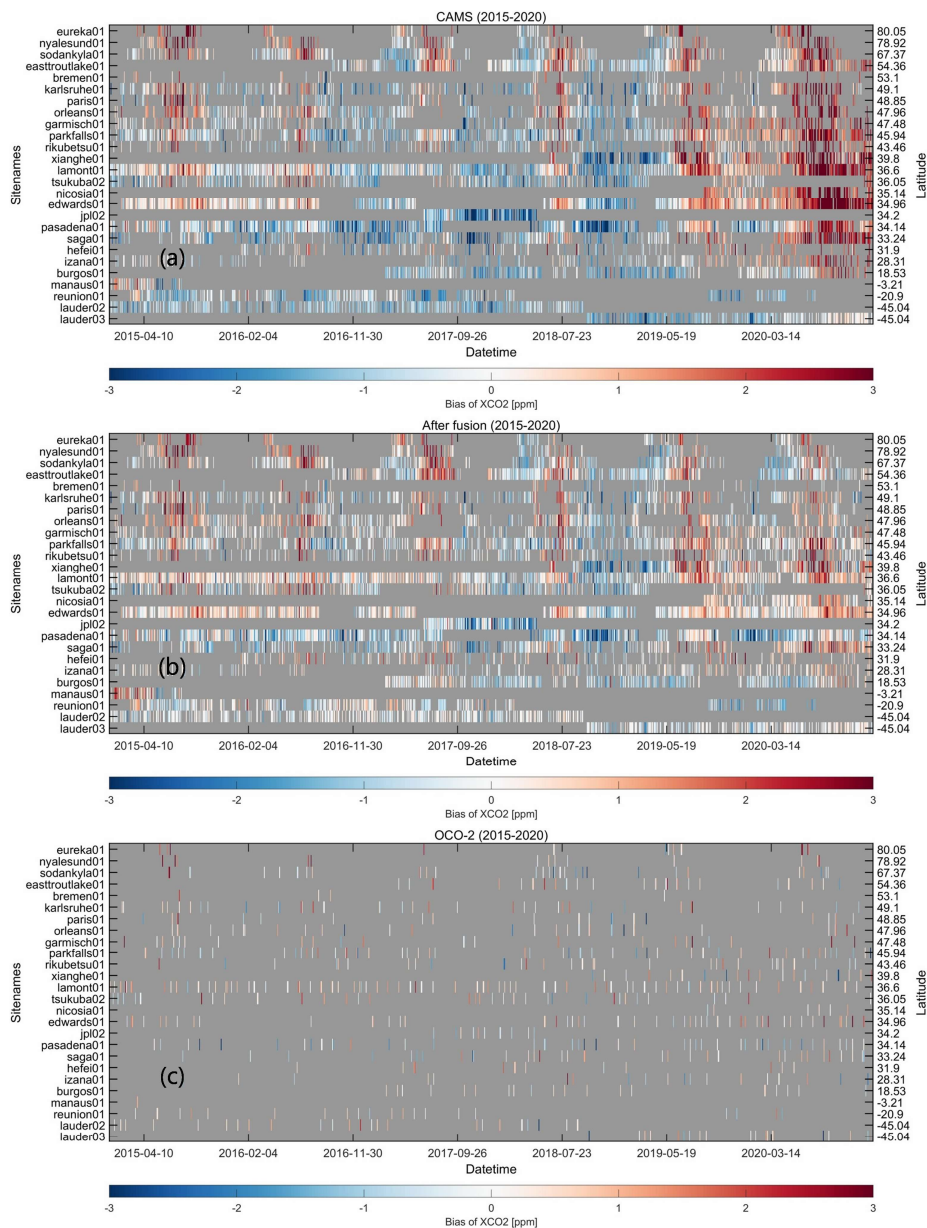


269
270 **Figure 7.** Scatter-plots of the time series for daily CAMS-EGG4, GOSAT, OCO-2, fused, and TCCON data on lauder02. The first and second
271 numbers in the bracket represent μ and σ , respectively. Unit: ppm/ppb to XCO_2/XCH_4 for μ and σ .



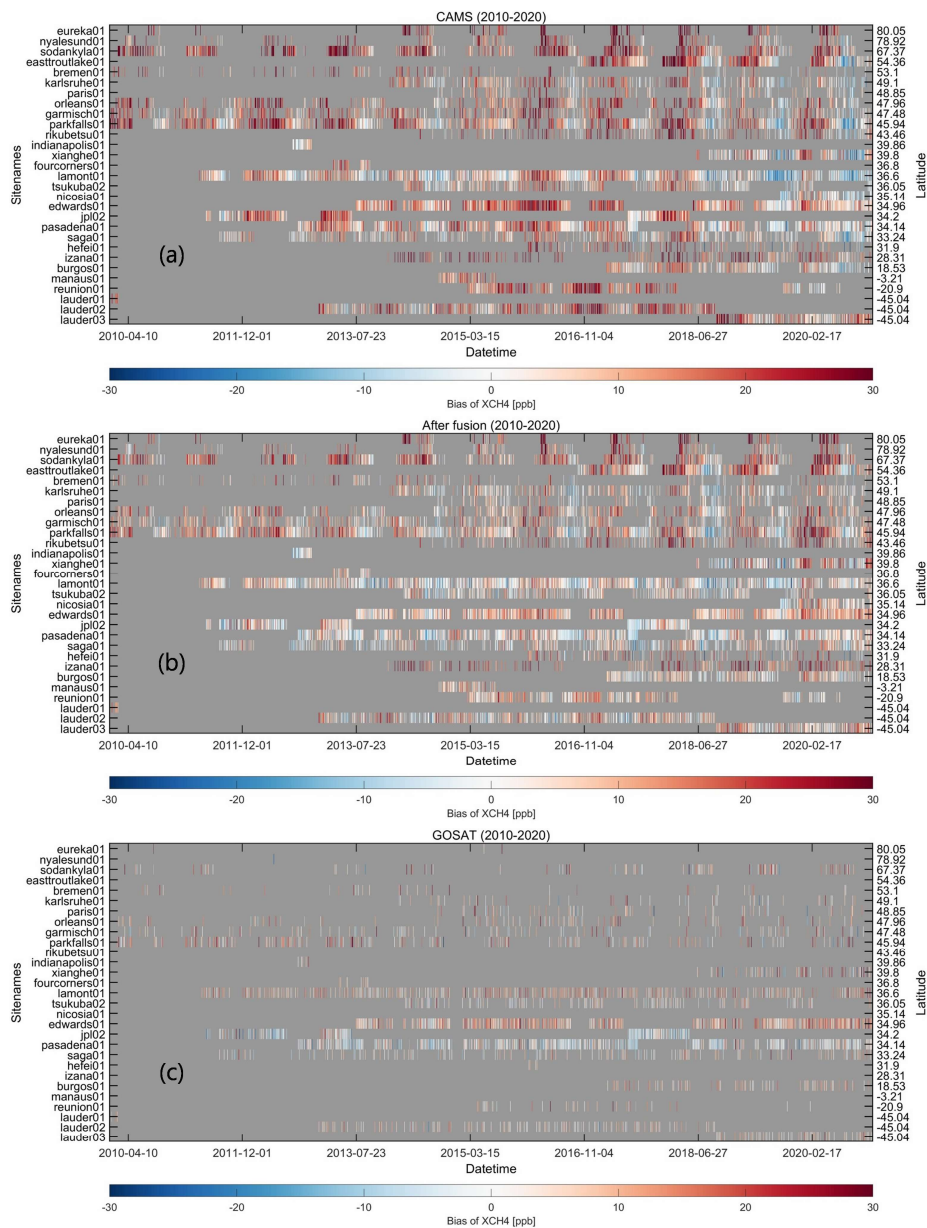
272

273 **Figure 8.** Heat maps of the biases between daily (a) CAMS-EGG4/(b) fused/(c) GOSAT and TCCON XCO₂ over time and latitude. Color
274 ramps stand for the biases of XCO₂. Background colors (grey) indicate the missing data.



275

276 **Figure 9.** Heat maps of the biases between daily (a) CAMS-EGG4/(b) fused/(c) OCO-2 and TCCON XCO₂ over time and latitude. Color
 277 ramps stand for the biases of XCO₂. Background colors (grey) indicate the missing data.



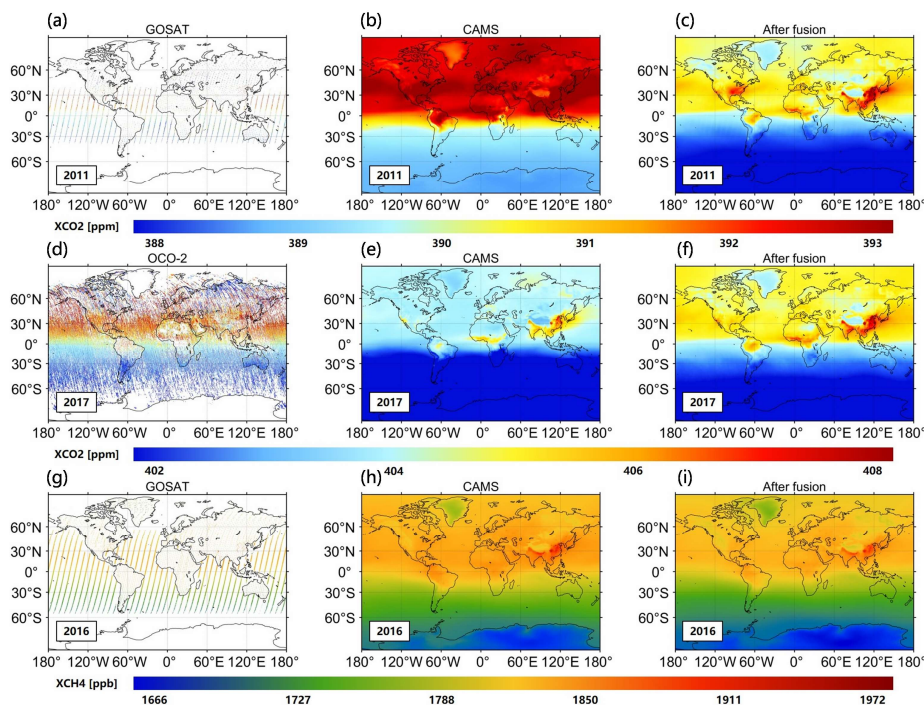
278

279 **Figure 10.** Heat maps of the biases between daily (a) CAMS-EGG4/(b) fused/(c) GOSAT and TCCON XCH₄ over time and latitude. Color
 280 ramps stand for the biases of XCO₂. Background colors (grey) indicate the missing data.

281 Figure 6, 7, and S25-S48 demonstrate the time series for daily CAMS-EGG4, GOSAT, OCO-2, fused, and TCCON data on
 282 each in-situ station. Similarly, two stations, i.e., garmisch01 and lauder02, are regarded as examples, which locate in Europe
 283 and Oceania, respectively. As depicted in Fig. 6, the XCO₂ from CAMS-EGG4 is markedly overestimated on garmisch01 from
 284 2010 to 2014 and in 2020. After fusion, the XCO₂ presents an equal trend compared to TCCON measurements over time, with
 285 smaller μ (0.096 and 0.139 ppm) and σ (1.067 and 1.01 ppm). In the meantime, the overestimation of CAMS-EGG4 XCH₄



286 is also mitigated on garmisch01 through our fusion method. Regarding lauder02, Figure 7 shows that CAMS-EGG4 generates
287 underestimated XCO₂ (2015-2019) and overestimated XCH₄. The μ and σ of the fused results (e.g., 4.952 and 10.189 ppb
288 for XCH₄) are significantly improved on lauder02. The time series on other stations are provided in the Supplement (see Fig.
289 S25-S48). The readers can refer to them if interested, which will not be further described here.



290
291 **Figure 11.** Annual (a and g) GOSAT, (d) OCO-2, (b, e, and h) CAMS-EGG4, and (c, f, and i) fused XCO₂/XCH₄ over the globe. Color
292 ramps stand for the values of XCO₂ and XCH₄.

293 4.3 Uncertainty analyses

294 Figure 8-10 display the biases between daily CAMS-EGG4/fused/GOSAT/OCO-2 and TCCON data over time and latitude.
295 As observed in Fig. 8 and 9, a large overestimation generally exists in the CAMS-EGG4 XCO₂ from 2010 to 2014 and in 2020,
296 especially before 2013 and in 2020 (> 3 ppm). These are attributed to the considerable errors in the satellite data assimilated
297 (2010-2014) and that anthropogenic emissions are not modified for COVID-19 lockdowns in 2020 (Agusti-Panareda et al.,
298 2022). After fusion, the biases of XCO₂ are well improved for most TCCON in-situ stations from 2010 to 2014 and in 2020,
299 whose patterns are similar to those of GOSAT and OCO-2 XCO₂, respectively. This indicates that the proposed fusion method
300 can effectively correct the biases in CAMS-EGG4 due to the issues from assimilation data. Meanwhile, CAMS-EGG4
301 generates distinctly underestimated XCO₂ from 2016 to 2019 on the stations of latitude < 40° N, which is also mitigated via
302 the S-STDCT fusion method (see Fig. 10). Moreover, the CAMS-EGG4 XCH₄ frequently presents a large positive bias (> 30
303 ppb), while the fused XCH₄ only enhances the performance on the stations of latitude < 50° N. The improvements for other

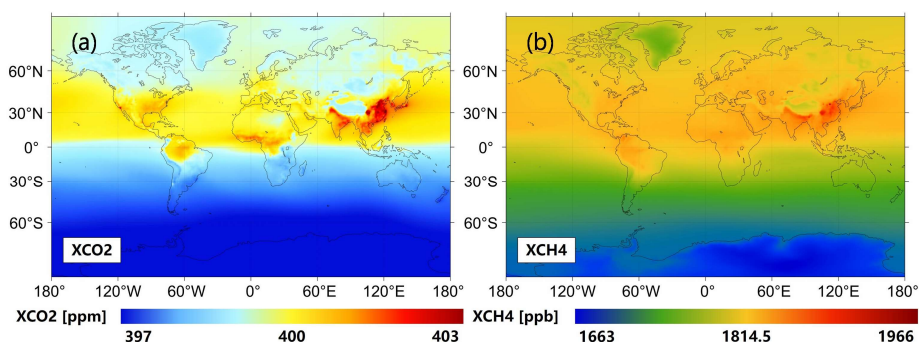


304 stations require our further efforts in the future.

305 4.4 Assessment of spatial distribution on multi-temporal scales

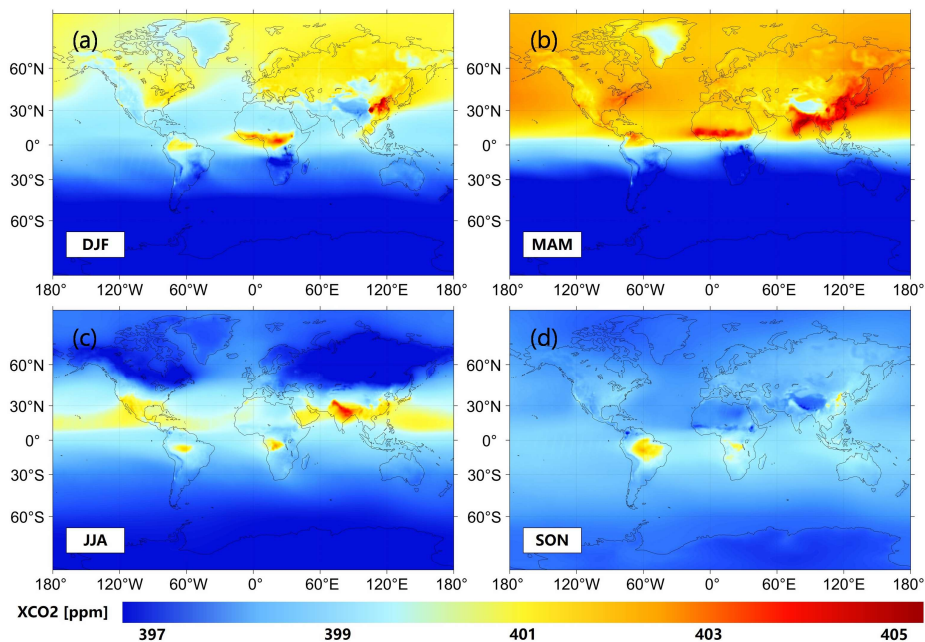
306 Figure 11 demonstrates the comparisons of annual GOSAT, OCO-2, CAMS-EGG4, and fused XCO_2/XCH_4 over the globe. A
307 total of three years are selected, including 2011, 2017, and 2016. As can be seen, the fused results present coincident spatial
308 patterns with GOSAT and OCO-2, even if the annual GOSAT and OCO-2 data are greatly sparse. Particularly, the large
309 overestimation and underestimation of CAMS-EGG4 XCO_2 in 2011 and 2017 are significantly modified after fusion,
310 respectively, which are mutually confirmed with the descriptions in Section 4.3.

311 Figure 12 depicts the multi-year mean fused global XCO_2 and XCH_4 from 2010 to 2020. Generally, the spatial patterns of
312 XCO_2 and XCH_4 are divided by the equator. The high values of XCO_2 and XCH_4 mainly distribute over Asia, e.g., China and
313 India, which is attributed to the large anthropogenic emissions (Kenea et al., 2023; Liu et al., 2020; Turner et al., 2015;
314 Hotchkiss et al., 2015). In the meantime, considerable natural emissions, e.g., wildfires (Arora and Melton, 2018), also can
315 obviously increase the XCO_2 values, such as in central Africa and northern South America. Figure 13 and 14 illustrate the
316 seasonal fused XCO_2 and XCH_4 from 2010 to 2020 over the globe, respectively. As displayed, seasonal changes of global
317 XCO_2 and XCH_4 spatial patterns are clearly reflected in the fused results. Compared to XCH_4 , the global spatial patterns of
318 XCO_2 vary more drastically. This is likely driven by the spatiotemporal heterogeneity of meteorological fields (Liu et al., 2011)
319 and different emission sources of CO_2 and CH_4 .



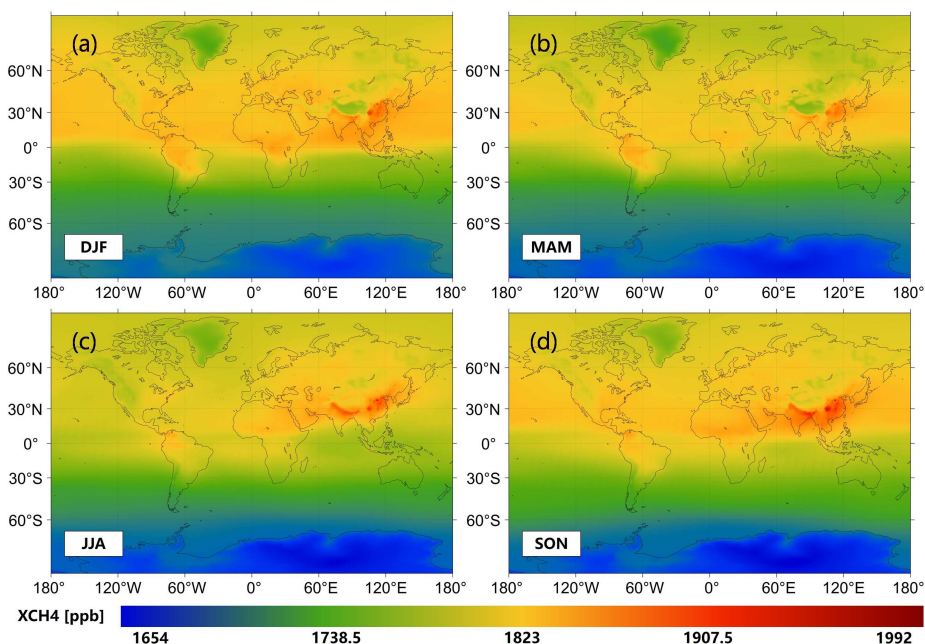
320

321 **Figure 12.** Multi-year mean fused (a) XCO_2 and (b) XCH_4 from 2010 to 2020 over the globe. Color ramps stand for the values of XCO_2 and
322 XCH_4 .



323

324 **Figure 13.** Seasonal fused XCO₂ from 2010 to 2020 over the globe. The color ramp stands for the value of XCO₂. (a) DJF, (b) MAM, (c)
325 JJA, and (d) SON denote Dec. to Feb., Mar. to May, Jun. to Aug., and Sep. to Nov., respectively.



326

327 **Figure 14.** Seasonal fused XCH₄ from 2010 to 2020 over the globe. The color ramp stands for the value of XCH₄. (a) DJF, (b) MAM, (c)
328 JJA, and (d) SON denote Dec. to Feb., Mar. to May, Jun. to Aug., and Sep. to Nov., respectively.

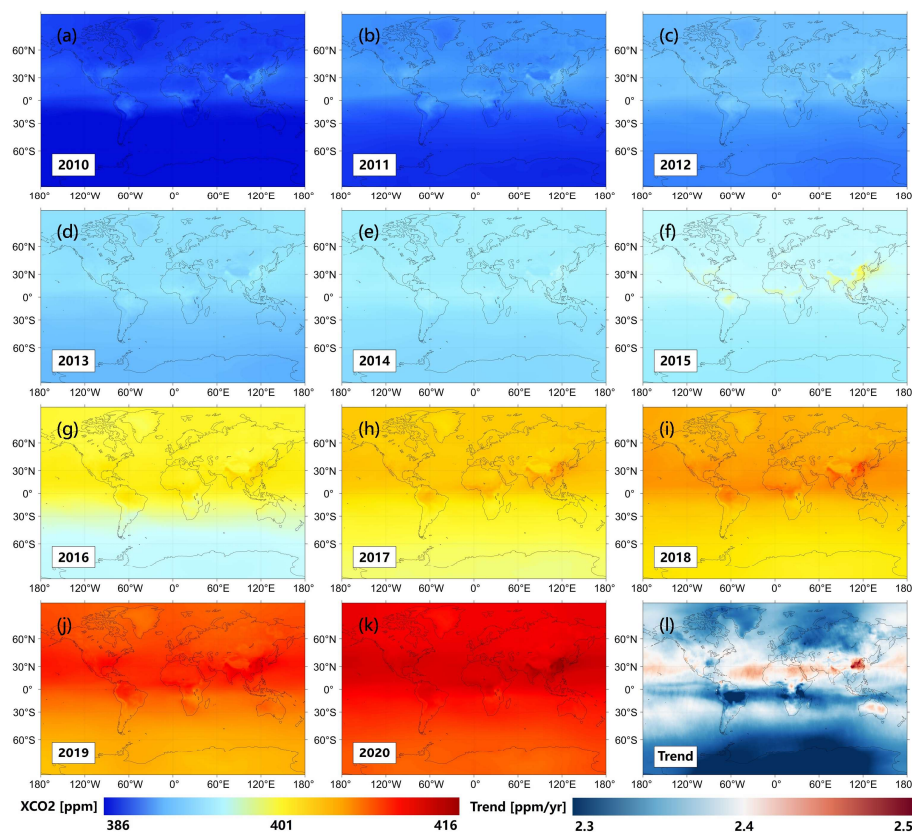
329 Figure 15 and 16 map the annual fused global XCO₂ and XCH₄ from 2010 to 2020, respectively, including their trends. As



330 observed in Fig. 15, the CO₂ levels continuously increase from 2010 to 2020, with the mean XCO₂ values ranging from ≤
331 386 to ≥ 416 ppm. However, the trends of XCO₂ only present small spatial differences (~ 0.2 ppm per year), of which the
332 large growth rates primarily distribute along the equator, especially for China (≥ 2.5 ppm per year). It is worth noting that the
333 growth rates of XCO₂ are relatively slight (≤ 2.3 ppm per year) in northern South America compared to other regions. This is
334 likely caused by the effects from the carbon sequestration of forests (Chazdon et al., 2016). Besides, the XCH₄ values also
335 notably rise from 2010 to 2020, of which the maximum is not less than 2008 ppb in 2020 (see Fig. 16). The large growth rates
336 of XCH₄ are majorly discovered over southern Asia and northern Europe.

337 5 Data availability

338 The fused results can be freely accessed at <http://doi.org/10.5281/zenodo.7388893> (Wang et al., 2022b). The daily global
339 seamless gridded (0.25°) XCO₂ and XCH₄ from 2010 to 2020 are stored in the netCDF4 format with a file size of ~ 3.5 MB
340 for each day. The units of XCO₂ and XCH₄ are ppm and ppb, respectively.

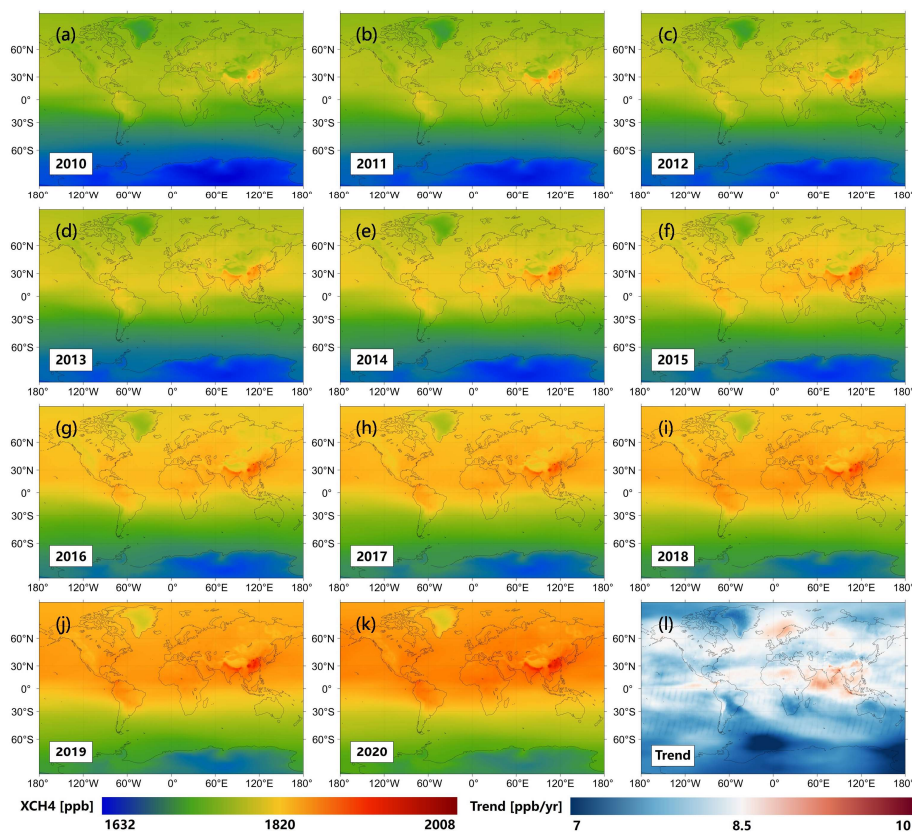


341
342 **Figure 15.** Annual fused (a-k) XCO₂ and (l) its trend from 2010 to 2020 over the globe. Color ramps stand for the values of XCO₂ and its
343 trend, ppm/yr: ppm per year.



344 6 Conclusions

345 In our study, a novel spatiotemporally self-supervised fusion method, i.e., S-STDCT, is proposed to acquire long-term daily
346 seamless globally distributed XCO₂ and XCH₄ products from 2010 to 2020 at the grids of 0.25°. A total of three datasets are
347 adopted, which include GOSAT, OCO-2, and CAMS-EGG4. Since the data from GOSAT and OCO-2 is greatly sparse in
348 space-time domain, the algorithm for frequency domain (the *STDCT*) is applied in the fusion task. Validation results show that
349 the S-STDCT fusion method performs well over the globe, with the σ (R^2) of ~ 1.18 ppm (0.91 or 0.95) and 11.3 ppb (0.9)
350 for XCO₂ and XCH₄ against TCCON measurements, respectively. Generally, the accuracy of fused results is distinctly superior
351 to that of CAMS-EGG4, which also exceeds or equals those of GSOAT and OCO-2. Particularly, the proposed fusion method
352 effectively modifies the large biases in CAMS-EGG4 caused by the issues from assimilation data, such as the uncorrected
353 anthropogenic emission inventories for COVID-19 lockdowns in 2020. Besides, the spatial patterns of fused results remain
354 coincident with GOSAT and OCO-2, which can accurately display the long-term and seasonal changes of global XCO₂ and
355 XCH₄ spatial distribution. The long-term (2010-2020) daily global seamless gridded (0.25°) fused results are available at
356 <http://doi.org/10.5281/zenodo.7388893> (Wang et al., 2022b).



357
358 **Figure 16.** Annual fused (a-k) XCH₄ and (l) its trend from 2010 to 2020 over the globe. Color ramps stand for the values of XCH₄ and its
359 trend. ppb/yr: ppb per year.



360 **Author contributions**

361 YW designed the study, collected and processed the data, analyzed the results, and wrote the paper. QQY and TWL provided
362 constructive comments on the paper. YJY, SQZ, and LPZ revised the paper. All authors contributed to the study.

363 **Competing interests**

364 The contact author has declared that none of the authors has any competing interests.

365 **Disclaimer**

366 Publisher's note: Copernicus Publications remains neutral with regard to jurisdictional claims in published maps and
367 institutional affiliations.

368 **Acknowledgments**

369 The authors would like to express gratitude to the Goddard Earth Science Data and Information Services Center for providing
370 the GOSAT and OCO-2 XCO₂ products (last access: 20 November 2022 and 27 November 2022), the Centre for
371 Environmental Data Analysis for providing the GOSAT XCH₄ product (last access: 18 November 2022), the Copernicus
372 Climate Data Store for providing the CAMS-EGG4 XCO₂ and XCH₄ products (last access: 25 November 2022), the Total
373 Carbon Column Observing Network (hosted by CaltechDATA at <https://tcondata.org>; Chair: Dr. Debra Wunch) for
374 establishing and maintaining in-situ stations (last access: 18 November 2022).

375 **Financial support**

376 Our work is supported by the National Natural Science Foundation of China (No. 41922008), the Basic and Applied Basic
377 Research Foundation of Guangdong Province (No. 2021A1515110567), and the Hubei Science Foundation for Distinguished
378 Young Scholars (No. 2020CFA051).

379 **References**

380 Agusti-Panareda, A., Barré, J., Massart, S., Inness, A., Aben, I., Ades, M., Baier, B. C., Balsamo, G., Borsdorff, T.,
381 Bousserez, N., Boussetta, S., Buchwitz, M., Cantarello, L., Crevoisier, C., Engelen, R., Eskes, H., Flemming, J.,
382 Garrigues, S., Hasekamp, O., Huijnen, V., Jones, L., Kipling, Z., Langerock, B., McNorton, J., Meilhac, N., Noel, S.,
383 Parrington, M., Peuch, V.-H., Ramonet, M., Ratzinger, M., Reuter, M., Ribas, R., Suttie, M., Sweeney, C., Tarniewicz,
384 J., and Wu, L.: Technical note: The CAMS greenhouse gas reanalysis from 2003 to 2020, EGU sphere, 1–51,
385 <https://doi.org/10.5194/egusphere-2022-283>, 2022.

386 Arora, V. K. and Melton, J. R.: Reduction in global area burned and wildfire emissions since 1930s enhances carbon



- 387 uptake by land, *Nat Commun*, 9, 1326, <https://doi.org/10.1038/s41467-018-03838-0>, 2018.
- 388 August, T., Klaes, D., Schlüssel, P., Hultberg, T., Crapeau, M., Arriaga, A., O'Carroll, A., Coppens, D., Munro, R., and
389 Calbet, X.: IASI on Metop-A: Operational Level 2 retrievals after five years in orbit, *Journal of Quantitative*
390 *Spectroscopy and Radiative Transfer*, 113, 1340–1371, <https://doi.org/10.1016/j.jqsrt.2012.02.028>, 2012.
- 391 Battin, T. J., Luysaert, S., Kaplan, L. A., Aufdenkampe, A. K., Richter, A., and Tranvik, L. J.: The boundless carbon
392 cycle, *Nature Geosci*, 2, 598–600, <https://doi.org/10.1038/ngeo618>, 2009.
- 393 Beirle, S., Lampel, J., Wang, Y., Mies, K., Dörner, S., Grossi, M., Loyola, D., Dehn, A., Danielczok, A., Schröder, M.,
394 and Wagner, T.: The ESA GOME-Evolution “Climate” water vapor product: a homogenized time series of H₂O columns
395 from GOME, SCIAMACHY, and GOME-2, *Earth System Science Data*, 10, 449–468, [https://doi.org/10.5194/essd-10-](https://doi.org/10.5194/essd-10-396-449-2018)
396 449-2018, 2018.
- 397 Bergamaschi, P., Houweling, S., Segers, A., Krol, M., Frankenberg, C., Scheepmaker, R. A., Dlugokencky, E., Wofsy, S.
398 C., Kort, E. A., Sweeney, C., Schuck, T., Brenninkmeijer, C., Chen, H., Beck, V., and Gerbig, C.: Atmospheric CH₄ in
399 the first decade of the 21st century: Inverse modeling analysis using SCIAMACHY satellite retrievals and NOAA surface
400 measurements, *Journal of Geophysical Research: Atmospheres*, 118, 7350–7369, <https://doi.org/10.1002/jgrd.50480>,
401 2013.
- 402 Bhattacharjee, S., Mitra, P., and Ghosh, S. K.: Spatial Interpolation to Predict Missing Attributes in GIS Using Semantic
403 Kriging, *IEEE Transactions on Geoscience and Remote Sensing*, 52, 4771–4780,
404 <https://doi.org/10.1109/TGRS.2013.2284489>, 2014.
- 405 Buchwitz, M., Reuter, M., Schneising, O., Boesch, H., Guerlet, S., Dils, B., Aben, I., Armante, R., Bergamaschi, P.,
406 Blumenstock, T., Bovensmann, H., Brunner, D., Buchmann, B., Burrows, J. P., Butz, A., Chédin, A., Chevallier, F.,
407 Crevoisier, C. D., Deutscher, N. M., Frankenberg, C., Hase, F., Hasekamp, O. P., Heymann, J., Kaminski, T., Laeng, A.,
408 Lichtenberg, G., De Mazière, M., Noël, S., Notholt, J., Orphal, J., Popp, C., Parker, R., Scholze, M., Sussmann, R., Stiller,
409 G. P., Warneke, T., Zehner, C., Bril, A., Crisp, D., Griffith, D. W. T., Kuze, A., O'Dell, C., Oshchepkov, S., Sherlock, V.,
410 Suto, H., Wennberg, P., Wunch, D., Yokota, T., and Yoshida, Y.: The Greenhouse Gas Climate Change Initiative (GHG-
411 CCI): Comparison and quality assessment of near-surface-sensitive satellite-derived CO₂ and CH₄ global data sets,
412 *Remote Sensing of Environment*, 162, 344–362, <https://doi.org/10.1016/j.rse.2013.04.024>, 2015.
- 413 Burrows, J. P., Hölzle, E., Goede, A. P. H., Visser, H., and Fricke, W.: SCIAMACHY—scanning imaging absorption
414 spectrometer for atmospheric chartography, *Acta Astronautica*, 35, 445–451, [https://doi.org/10.1016/0094-](https://doi.org/10.1016/0094-415-5765(94)00278-T)
415 5765(94)00278-T, 1995.
- 416 Chazdon, R. L., Broadbent, E. N., Rozendaal, D. M. A., Bongers, F., Zambrano, A. M. A., Aide, T. M., Balvanera, P.,
417 Becknell, J. M., Boukili, V., Brancalion, P. H. S., Craven, D., Almeida-Cortez, J. S., Cabral, G. A. L., de Jong, B.,
418 Denslow, J. S., Dent, D. H., DeWalt, S. J., Dupuy, J. M., Durán, S. M., Espírito-Santo, M. M., Fandino, M. C., César, R.
419 G., Hall, J. S., Hernández-Stefanoni, J. L., Jakovac, C. C., Junqueira, A. B., Kennard, D., Letcher, S. G., Lohbeck, M.,
420 Martínez-Ramos, M., Massoca, P., Meave, J. A., Mesquita, R., Mora, F., Muñoz, R., Muscarella, R., Nunes, Y. R. F.,
421 Ochoa-Gaona, S., Orihuela-Belmonte, E., Peña-Claros, M., Pérez-García, E. A., Piotto, D., Powers, J. S., Rodríguez-
422 Velazquez, J., Romero-Pérez, I. E., Ruíz, J., Saldarriaga, J. G., Sanchez-Azofeifa, A., Schwartz, N. B., Steininger, M. K.,
423 Swenson, N. G., Uriarte, M., van Breugel, M., van der Wal, H., Veloso, M. D. M., Vester, H., Vieira, I. C. G., Bentos, T.
424 V., Williamson, G. B., and Poorter, L.: Carbon sequestration potential of second-growth forest regeneration in the Latin
425 American tropics, *Science Advances*, 2, e1501639, <https://doi.org/10.1126/sciadv.1501639>, 2016.
- 426 Chen, H., Xu, X., Fang, C., Li, B., and Nie, M.: Differences in the temperature dependence of wetland CO₂ and CH₄



- 427 emissions vary with water table depth, *Nat. Clim. Chang.*, 11, 766–771, <https://doi.org/10.1038/s41558-021-01108-4>,
428 2021.
- 429 Choulga, M., Janssens-Maenhout, G., Super, I., Solazzo, E., Agusti-Panareda, A., Balsamo, G., Bousserez, N., Crippa,
430 M., Denier van der Gon, H., Engelen, R., Guizzardi, D., Kuenen, J., McNorton, J., Oreggioni, G., and Visschedijk, A.:
431 Global anthropogenic CO₂ emissions and uncertainties as a prior for Earth system modelling and data assimilation, *Earth*
432 *System Science Data*, 13, 5311–5335, <https://doi.org/10.5194/essd-13-5311-2021>, 2021.
- 433 Cintra, R. J. and Bayer, F. M.: A DCT Approximation for Image Compression, *IEEE Signal Processing Letters*, 18, 579–
434 582, <https://doi.org/10.1109/LSP.2011.2163394>, 2011.
- 435 Crisp, D., Pollock, H. R., Rosenberg, R., Chapsky, L., Lee, R. A. M., Oyafuso, F. A., Frankenberg, C., O'Dell, C. W.,
436 Bruegge, C. J., Doran, G. B., Eldering, A., Fisher, B. M., Fu, D., Gunson, M. R., Mandrake, L., Osterman, G. B.,
437 Schwandner, F. M., Sun, K., Taylor, T. E., Wennberg, P. O., and Wunch, D.: The on-orbit performance of the Orbiting
438 Carbon Observatory-2 (OCO-2) instrument and its radiometrically calibrated products, *Atmospheric Measurement*
439 *Techniques*, 10, 59–81, <https://doi.org/10.5194/amt-10-59-2017>, 2017.
- 440 Crosswell, J. R., Anderson, I. C., Stanhope, J. W., Van Dam, B., Brush, M. J., Ensign, S., Piehler, M. F., McKee, B., Bost,
441 M., and Paerl, H. W.: Carbon budget of a shallow, lagoonal estuary: Transformations and source-sink dynamics along
442 the river-estuary-ocean continuum, *Limnology and Oceanography*, 62, S29–S45, <https://doi.org/10.1002/lno.10631>,
443 2017.
- 444 Deng, F., Jones, D. B. A., Henze, D. K., Bousserez, N., Bowman, K. W., Fisher, J. B., Nassar, R., O'Dell, C., Wunch, D.,
445 Wennberg, P. O., Kort, E. A., Wofsy, S. C., Blumenstock, T., Deutscher, N. M., Griffith, D. W. T., Hase, F., Heikkinen,
446 P., Sherlock, V., Strong, K., Sussmann, R., and Warneke, T.: Inferring regional sources and sinks of atmospheric CO₂
447 from GOSAT XCO₂ data, *Atmospheric Chemistry and Physics*, 14, 3703–3727, [https://doi.org/10.5194/acp-14-3703-](https://doi.org/10.5194/acp-14-3703-448)
448 2014, 2014.
- 449 Doughty, R., Kurosu, T. P., Parazoo, N., Köhler, P., Wang, Y., Sun, Y., and Frankenberg, C.: Global GOSAT, OCO-2, and
450 OCO-3 solar-induced chlorophyll fluorescence datasets, *Earth System Science Data*, 14, 1513–1529,
451 <https://doi.org/10.5194/essd-14-1513-2022>, 2022.
- 452 El-Mahallawy, M. S. and Hashim, M.: Material Classification of Underground Utilities From GPR Images Using DCT-
453 Based SVM Approach, *IEEE Geoscience and Remote Sensing Letters*, 10, 1542–1546,
454 <https://doi.org/10.1109/LGRS.2013.2261796>, 2013.
- 455 Fraser, A., Palmer, P. I., Feng, L., Boesch, H., Cogan, A., Parker, R., Dlugokencky, E. J., Fraser, P. J., Krummel, P. B.,
456 Langenfelds, R. L., O'Doherty, S., Prinn, R. G., Steele, L. P., van der Schoot, M., and Weiss, R. F.: Estimating regional
457 methane surface fluxes: the relative importance of surface and GOSAT mole fraction measurements, *Atmospheric*
458 *Chemistry and Physics*, 13, 5697–5713, <https://doi.org/10.5194/acp-13-5697-2013>, 2013.
- 459 Fredj, E., Roarty, H., Kohut, J., Smith, M., and Glenn, S.: Gap Filling of the Coastal Ocean Surface Currents from HFR
460 Data: Application to the Mid-Atlantic Bight HFR Network, *Journal of Atmospheric and Oceanic Technology*, 33, 1097–
461 1111, <https://doi.org/10.1175/JTECH-D-15-0056.1>, 2016.
- 462 Garcia, D.: Robust smoothing of gridded data in one and higher dimensions with missing values, *Computational*
463 *Statistics & Data Analysis*, 54, 1167–1178, <https://doi.org/10.1016/j.csda.2009.09.020>, 2010.
- 464 Hakkarainen, J., Ialongo, I., and Tamminen, J.: Direct space-based observations of anthropogenic CO₂ emission areas
465 from OCO-2, *Geophysical Research Letters*, 43, 11,400–11,406, <https://doi.org/10.1002/2016GL070885>, 2016.



- 466 Hamazaki, T., Kaneko, Y., Kuze, A., and Kondo, K.: Fourier transform spectrometer for Greenhouse Gases Observing
467 Satellite (GOSAT), in: Enabling Sensor and Platform Technologies for Spaceborne Remote Sensing, Enabling Sensor
468 and Platform Technologies for Spaceborne Remote Sensing, 73–80, <https://doi.org/10.1117/12.581198>, 2005.
- 469 He, C., Ji, M., Grieneisen, M. L., and Zhan, Y.: A review of datasets and methods for deriving spatiotemporal distributions
470 of atmospheric CO₂, *Journal of Environmental Management*, 322, 116101,
471 <https://doi.org/10.1016/j.jenvman.2022.116101>, 2022a.
- 472 He, C., Ji, M., Li, T., Liu, X., Tang, D., Zhang, S., Luo, Y., Grieneisen, M. L., Zhou, Z., and Zhan, Y.: Deriving Full-
473 Coverage and Fine-Scale XCO₂ Across China Based on OCO-2 Satellite Retrievals and CarbonTracker Output,
474 *Geophysical Research Letters*, 49, e2022GL098435, <https://doi.org/10.1029/2022GL098435>, 2022b.
- 475 He, Z., Lei, L., Zhang, Y., Sheng, M., Wu, C., Li, L., Zeng, Z.-C., and Welp, L. R.: Spatio-Temporal Mapping of Multi-
476 Satellite Observed Column Atmospheric CO₂ Using Precision-Weighted Kriging Method, *Remote Sensing*, 12, 576,
477 <https://doi.org/10.3390/rs12030576>, 2020.
- 478 Hong, X., Zhang, P., Bi, Y., Liu, C., Sun, Y., Wang, W., Chen, Z., Yin, H., Zhang, C., Tian, Y., and Liu, J.: Retrieval of
479 Global Carbon Dioxide From TanSat Satellite and Comprehensive Validation With TCCON Measurements and Satellite
480 Observations, *IEEE Transactions on Geoscience and Remote Sensing*, 60, 1–16,
481 <https://doi.org/10.1109/TGRS.2021.3066623>, 2022.
- 482 Hotchkiss, E. R., Hall Jr, R. O., Sponseller, R. A., Butman, D., Klaminder, J., Laudon, H., Rosvall, M., and Karlsson, J.:
483 Sources of and processes controlling CO₂ emissions change with the size of streams and rivers, *Nature Geosci*, 8, 696–
484 699, <https://doi.org/10.1038/ngeo2507>, 2015.
- 485 Houweling, S., Baker, D., Basu, S., Boesch, H., Butz, A., Chevallier, F., Deng, F., Dlugokencky, E. J., Feng, L., Ganshin,
486 A., Hasekamp, O., Jones, D., Maksyutov, S., Marshall, J., Oda, T., O’Dell, C. W., Oshchepkov, S., Palmer, P. I., Peylin,
487 P., Poussi, Z., Reum, F., Takagi, H., Yoshida, Y., and Zhuravlev, R.: An intercomparison of inverse models for estimating
488 sources and sinks of CO₂ using GOSAT measurements, *Journal of Geophysical Research: Atmospheres*, 120, 5253–
489 5266, <https://doi.org/10.1002/2014JD022962>, 2015.
- 490 Jiang, F., Ju, W., He, W., Wu, M., Wang, H., Wang, J., Jia, M., Feng, S., Zhang, L., and Chen, J. M.: A 10-year global
491 monthly averaged terrestrial net ecosystem exchange dataset inferred from the ACOS GOSAT v9 XCO₂ retrievals
492 (GCAS2021), *Earth System Science Data*, 14, 3013–3037, <https://doi.org/10.5194/essd-14-3013-2022>, 2022.
- 493 Katzfuss, M. and Cressie, N.: Tutorial on fixed rank kriging (FRK) of CO₂ data, Department of Statistics, The Ohio
494 State University, Columbus, 2011.
- 495 Kenea, S. T., Lee, H., Patra, P. K., Li, S., Labzovskii, L. D., and Joo, S.: Long-term changes in CH₄ emissions:
496 Comparing $\Delta\text{CH}_4/\Delta\text{CO}_2$ ratios between observation and proved model in East Asia (2010–2020), *Atmospheric*
497 *Environment*, 293, 119437, <https://doi.org/10.1016/j.atmosenv.2022.119437>, 2023.
- 498 Kiel, M., O’Dell, C. W., Fisher, B., Eldering, A., Nassar, R., MacDonald, C. G., and Wennberg, P. O.: How bias correction
499 goes wrong: measurement of X_{CO₂} affected by erroneous surface pressure estimates, *Atmospheric Measurement*
500 *Techniques*, 12, 2241–2259, <https://doi.org/10.5194/amt-12-2241-2019>, 2019.
- 501 Laughner, J. L., Roche, S., Kiel, M., Toon, G. C., Wunch, D., Baier, B. C., Biraud, S., Chen, H., Kivi, R., Laemmel, T.,
502 McKain, K., Quéhé, P.-Y., Rousogonous, C., Stephens, B. B., Walker, K., and Wennberg, P. O.: A new algorithm to
503 generate a priori trace gas profiles for the GGG2020 retrieval algorithm, *Atmospheric Measurement Techniques*
504 *Discussions*, 1–41, <https://doi.org/10.5194/amt-2022-267>, 2022.



- 505 Le Quéré, C., Korsbakken, J. I., Wilson, C., Tosun, J., Andrew, R., Andres, R. J., Canadell, J. G., Jordan, A., Peters, G.
506 P., and van Vuuren, D. P.: Drivers of declining CO₂ emissions in 18 developed economies, *Nat. Clim. Chang.*, 9, 213–
507 217, <https://doi.org/10.1038/s41558-019-0419-7>, 2019.
- 508 Li, L., Lei, L., Song, H., Zeng, Z., and He, Z.: Spatiotemporal Geostatistical Analysis and Global Mapping of CH₄
509 Columns from GOSAT Observations, *Remote Sensing*, 14, 654, <https://doi.org/10.3390/rs14030654>, 2022.
- 510 Lin, X., Zhang, W., Crippa, M., Peng, S., Han, P., Zeng, N., Yu, L., and Wang, G.: A comparative study of anthropogenic
511 CH₄ emissions over China based on the ensembles of bottom-up inventories, *Earth System Science Data*, 13, 1073–1088,
512 <https://doi.org/10.5194/essd-13-1073-2021>, 2021.
- 513 Liu, J., Fung, I., Kalnay, E., and Kang, J.-S.: CO₂ transport uncertainties from the uncertainties in meteorological fields,
514 *Geophysical Research Letters*, 38, <https://doi.org/10.1029/2011GL047213>, 2011.
- 515 Liu, L. and Greaver, T. L.: A review of nitrogen enrichment effects on three biogenic GHGs: the CO₂ sink may be largely
516 offset by stimulated N₂O and CH₄ emission, *Ecology Letters*, 12, 1103–1117, <https://doi.org/10.1111/j.1461-0248.2009.01351.x>, 2009.
- 518 Liu, Y., Wang, J., Yao, L., Chen, X., Cai, Z., Yang, D., Yin, Z., Gu, S., Tian, L., Lu, N., and Lyu, D.: The TanSat mission:
519 preliminary global observations, *Science Bulletin*, 63, 1200–1207, <https://doi.org/10.1016/j.scib.2018.08.004>, 2018.
- 520 Liu, Z., Liu, Z., Song, T., Gao, W., Wang, Y., Wang, L., Hu, B., Xin, J., and Wang, Y.: Long-term variation in CO₂
521 emissions with implications for the interannual trend in PM_{2.5} over the last decade in Beijing, China, *Environmental*
522 *Pollution*, 266, 115014, <https://doi.org/10.1016/j.envpol.2020.115014>, 2020.
- 523 Meinshausen, M., Meinshausen, N., Hare, W., Raper, S. C. B., Frieler, K., Knutti, R., Frame, D. J., and Allen, M. R.:
524 Greenhouse-gas emission targets for limiting global warming to 2 °C, *Nature*, 458, 1158–1162,
525 <https://doi.org/10.1038/nature08017>, 2009.
- 526 Montzka, S. A., Dlugokencky, E. J., and Butler, J. H.: Non-CO₂ greenhouse gases and climate change, *Nature*, 476, 43–
527 50, <https://doi.org/10.1038/nature10322>, 2011.
- 528 Moran, D., Pichler, P.-P., Zheng, H., Muri, H., Klenner, J., Kramel, D., Többen, J., Weisz, H., Wiedmann, T., Wyckmans,
529 A., Strømman, A. H., and Gurney, K. R.: Estimating CO₂ emissions for 108 000 European cities, *Earth System*
530 *Science Data*, 14, 845–864, <https://doi.org/10.5194/essd-14-845-2022>, 2022.
- 531 Mueller, T. G., Pusuluri, N. B., Mathias, K. K., Cornelius, P. L., Barnhisel, R. I., and Shearer, S. A.: Map quality for
532 ordinary kriging and inverse distance weighted interpolation, *Soil Science Society of America Journal*, 68, 2042–2047,
533 2004.
- 534 Parker, R. J., Webb, A., Boesch, H., Somkuti, P., Barrio Guillo, R., Di Noia, A., Kalaitzi, N., Anand, J. S., Bergamaschi,
535 P., Chevallier, F., Palmer, P. I., Feng, L., Deutscher, N. M., Feist, D. G., Griffith, D. W. T., Hase, F., Kivi, R., Morino, I.,
536 Notholt, J., Oh, Y.-S., Ohyama, H., Petri, C., Pollard, D. F., Roehl, C., Sha, M. K., Shiomi, K., Strong, K., Sussmann, R.,
537 Té, Y., Velasco, V. A., Warneke, T., Wennberg, P. O., and Wunch, D.: A decade of GOSAT Proxy satellite CH₄
538 observations, *Earth System Science Data*, 12, 3383–3412, <https://doi.org/10.5194/essd-12-3383-2020>, 2020.
- 539 Petrescu, A. M. R., Qiu, C., Ciais, P., Thompson, R. L., Peylin, P., McGrath, M. J., Solazzo, E., Janssens-Maenhout, G.,
540 Tubiello, F. N., Bergamaschi, P., Brunner, D., Peters, G. P., Höglund-Isaksson, L., Regnier, P., Lauerwald, R., Bastviken,
541 D., Tsuruta, A., Winiwarter, W., Patra, P. K., Kuhnert, M., Oreggioni, G. D., Crippa, M., Saunois, M., Perugini, L.,
542 Markkanen, T., Aalto, T., Groot Zwaafink, C. D., Tian, H., Yao, Y., Wilson, C., Conchedda, G., Günther, D., Leip, A.,



- 543 Smith, P., Haussaire, J.-M., Leppänen, A., Manning, A. J., McNorton, J., Brockmann, P., and Dolman, A. J.: The
544 consolidated European synthesis of CH₄ and N₂O emissions for the European Union and United Kingdom: 1990–2017,
545 Earth System Science Data, 13, 2307–2362, <https://doi.org/10.5194/essd-13-2307-2021>, 2021.
- 546 Pham, H. T., Kim, S., Marshall, L., and Johnson, F.: Using 3D robust smoothing to fill land surface temperature gaps at
547 the continental scale, International Journal of Applied Earth Observation and Geoinformation, 82, 101879,
548 <https://doi.org/10.1016/j.jag.2019.05.012>, 2019.
- 549 Rao, K. R. and Yip, P.: Discrete Cosine Transform: Algorithms, Advantages, Applications, Academic Press, 517 pp.,
550 2014.
- 551 Reithmaier, G. M. S., Chen, X., Santos, I. R., Drexler, M. J., Holloway, C., Call, M., Álvarez, P. G., Euler, S., and Maher,
552 D. T.: Rainfall drives rapid shifts in carbon and nutrient source-sink dynamics of an urbanised, mangrove-fringed estuary,
553 Estuarine, Coastal and Shelf Science, 249, 107064, <https://doi.org/10.1016/j.ecss.2020.107064>, 2021.
- 554 Shine, K. P., Fuglestedt, J. S., Hailemariam, K., and Stuber, N.: Alternatives to the Global Warming Potential for
555 Comparing Climate Impacts of Emissions of Greenhouse Gases, Climatic Change, 68, 281–302,
556 <https://doi.org/10.1007/s10584-005-1146-9>, 2005.
- 557 Siabi, Z., Falahatkar, S., and Alavi, S. J.: Spatial distribution of XCO₂ using OCO-2 data in growing seasons, Journal of
558 Environmental Management, 244, 110–118, <https://doi.org/10.1016/j.jenvman.2019.05.049>, 2019.
- 559 Sjögersten, S., Black, C. R., Evers, S., Hoyos-Santillan, J., Wright, E. L., and Turner, B. L.: Tropical wetlands: A missing
560 link in the global carbon cycle?, Global Biogeochemical Cycles, 28, 1371–1386, <https://doi.org/10.1002/2014GB004844>,
561 2014.
- 562 Solomon, S., Daniel, J. S., Sanford, T. J., Murphy, D. M., Plattner, G.-K., Knutti, R., and Friedlingstein, P.: Persistence
563 of climate changes due to a range of greenhouse gases, Proceedings of the National Academy of Sciences, 107, 18354–
564 18359, <https://doi.org/10.1073/pnas.1006282107>, 2010.
- 565 Taylor, T. E., O’Dell, C. W., Frankenberg, C., Partain, P. T., Cronk, H. Q., Savtchenko, A., Nelson, R. R., Rosenthal, E.
566 J., Chang, A. Y., Fisher, B., Osterman, G. B., Pollock, R. H., Crisp, D., Eldering, A., and Gunson, M. R.: Orbiting Carbon
567 Observatory-2 (OCO-2) cloud screening algorithms: validation against collocated MODIS and CALIOP data,
568 Atmospheric Measurement Techniques, 9, 973–989, <https://doi.org/10.5194/amt-9-973-2016>, 2016.
- 569 Taylor, T. E., O’Dell, C. W., Crisp, D., Kuze, A., Lindqvist, H., Wennberg, P. O., Chatterjee, A., Gunson, M., Eldering,
570 A., Fisher, B., Kiel, M., Nelson, R. R., Merrelli, A., Osterman, G., Chevallier, F., Palmer, P. I., Feng, L., Deutscher, N.
571 M., Dubey, M. K., Feist, D. G., Garcia, O. E., Griffith, D. W. T., Hase, F., Iraci, L. T., Kivi, R., Liu, C., De Mazière, M.,
572 Morino, I., Notholt, J., Oh, Y.-S., Ohyama, H., Pollard, D. F., Rettinger, M., Schneider, M., Roehl, C. M., Sha, M. K.,
573 Shiomi, K., Strong, K., Sussmann, R., Té, Y., Velasco, V. A., Vrekoussis, M., Warneke, T., and Wunch, D.: An 11-year
574 record of XCO₂ estimates derived from GOSAT measurements using the NASA ACOS version 9 retrieval algorithm,
575 Earth System Science Data, 14, 325–360, <https://doi.org/10.5194/essd-14-325-2022>, 2022.
- 576 Turner, A. J., Jacob, D. J., Wecht, K. J., Maasakkers, J. D., Lundgren, E., Andrews, A. E., Biraud, S. C., Boesch, H.,
577 Bowman, K. W., Deutscher, N. M., Dubey, M. K., Griffith, D. W. T., Hase, F., Kuze, A., Notholt, J., Ohyama, H., Parker,
578 R., Payne, V. H., Sussmann, R., Sweeney, C., Velasco, V. A., Warneke, T., Wennberg, P. O., and Wunch, D.: Estimating
579 global and North American methane emissions with high spatial resolution using GOSAT satellite data, Atmospheric
580 Chemistry and Physics, 15, 7049–7069, <https://doi.org/10.5194/acp-15-7049-2015>, 2015.
- 581 Velasco, V. A., Deutscher, N. M., Morino, I., Uchino, O., Bukosa, B., Ajiro, M., Kamei, A., Jones, N. B., Paton-Walsh,



- 582 C., and Griffith, D. W. T.: Satellite and ground-based measurements of XCO₂ in a remote semiarid region of Australia,
583 Earth System Science Data, 11, 935–946, <https://doi.org/10.5194/essd-11-935-2019>, 2019.
- 584 Wang, G., Garcia, D., Liu, Y., de Jeu, R., and Johannes Dolman, A.: A three-dimensional gap filling method for large
585 geophysical datasets: Application to global satellite soil moisture observations, Environmental Modelling & Software,
586 30, 139–142, <https://doi.org/10.1016/j.envsoft.2011.10.015>, 2012.
- 587 Wang, H., Jiang, F., Wang, J., Ju, W., and Chen, J. M.: Terrestrial ecosystem carbon flux estimated using GOSAT and
588 OCO-2 XCO₂ retrievals, Atmospheric Chemistry and Physics, 19, 12067–12082, [https://doi.org/10.5194/acp-19-12067-](https://doi.org/10.5194/acp-19-12067-589)
589 2019, 2019.
- 590 Wang, T., Yu, P., Wu, Z., Lu, W., Liu, X., Li, Q. P., and Huang, B.: Revisiting the Intraseasonal Variability of Chlorophyll-
591 a in the Adjacent Luzon Strait With a New Gap-Filled Remote Sensing Data Set, IEEE Transactions on Geoscience and
592 Remote Sensing, 60, 1–11, <https://doi.org/10.1109/TGRS.2021.3067646>, 2022a.
- 593 Wang, Y., Yuan, Q., Li, T., Zhu, L., and Zhang, L.: Estimating daily full-coverage near surface O₃, CO, and NO₂
594 concentrations at a high spatial resolution over China based on S5P-TROPOMI and GEOS-FP, ISPRS Journal of
595 Photogrammetry and Remote Sensing, 175, 311–325, 2021a.
- 596 Wang, Y., Yuan, Q., Li, T., Zhu, L., and Zhang, L.: Estimating daily full-coverage near surface O₃, CO, and NO₂
597 concentrations at a high spatial resolution over China based on S5P-TROPOMI and GEOS-FP, ISPRS Journal of
598 Photogrammetry and Remote Sensing, 175, 311–325, 2021b.
- 599 Wang, Y., Yuan, Q., Li, T., and Zhang, L.: Global long-term (2010-2020) daily seamless fused XCO₂ and XCH₄ from
600 CAMS, OCO-2, and GOSAT, <https://doi.org/10.5281/zenodo.7388893>, 2022b.
- 601 Wang, Y., Yuan, Q., Li, T., and Zhu, L.: Global spatiotemporal estimation of daily high-resolution surface carbon
602 monoxide concentrations using Deep Forest, Journal of Cleaner Production, 350, 131500, 2022c.
- 603 Wu, L., Hasekamp, O., Hu, H., Landgraf, J., Butz, A., aan de Brugh, J., Aben, I., Pollard, D. F., Griffith, D. W. T., Feist,
604 D. G., Koshelev, D., Hase, F., Toon, G. C., Ohyama, H., Morino, I., Notholt, J., Shiomi, K., Iraci, L., Schneider, M., de
605 Mazière, M., Sussmann, R., Kivi, R., Warneke, T., Goo, T.-Y., and Té, Y.: Carbon dioxide retrieval from OCO-2 satellite
606 observations using the RemoTeC algorithm and validation with TCCON measurements, Atmospheric Measurement
607 Techniques, 11, 3111–3130, <https://doi.org/10.5194/amt-11-3111-2018>, 2018.
- 608 Wunch, D., Toon, G. C., Blavier, J.-F. L., Washenfelder, R. A., Notholt, J., Connor, B. J., Griffith, D. W. T., Sherlock, V.,
609 and Wennberg, P. O.: The Total Carbon Column Observing Network, Philosophical Transactions of the Royal Society A:
610 Mathematical, Physical and Engineering Sciences, 369, 2087–2112, <https://doi.org/10.1098/rsta.2010.0240>, 2011.
- 611 Wunch, D., Wennberg, P. O., Osterman, G., Fisher, B., Naylor, B., Roehl, C. M., O’Dell, C., Mandrake, L., Viatte, C.,
612 Kiel, M., Griffith, D. W. T., Deutscher, N. M., Velasco, V. A., Notholt, J., Warneke, T., Petri, C., De Maziere, M., Sha,
613 M. K., Sussmann, R., Rettinger, M., Pollard, D., Robinson, J., Morino, I., Uchino, O., Hase, F., Blumenstock, T., Feist,
614 D. G., Arnold, S. G., Strong, K., Mendonca, J., Kivi, R., Heikkinen, P., Iraci, L., Podolske, J., Hillyard, P. W., Kawakami,
615 S., Dubey, M. K., Parker, H. A., Sepulveda, E., García, O. E., Te, Y., Jeseck, P., Gunson, M. R., Crisp, D., and Eldering,
616 A.: Comparisons of the Orbiting Carbon Observatory-2 (OCO-2) XCO₂ measurements with TCCON, Atmospheric
617 Measurement Techniques, 10, 2209–2238, <https://doi.org/10.5194/amt-10-2209-2017>, 2017.
- 618 Yoro, K. O. and Daramola, M. O.: Chapter 1 - CO₂ emission sources, greenhouse gases, and the global warming effect,
619 in: Advances in Carbon Capture, edited by: Rahimpour, M. R., Farsi, M., and Makarem, M. A., Woodhead Publishing,
620 3–28, <https://doi.org/10.1016/B978-0-12-819657-1.00001-3>, 2020.



621 Yoshida, Y., Kikuchi, N., Morino, I., Uchino, O., Oshchepkov, S., Bril, A., Saeki, T., Schutgens, N., Toon, G. C., Wunch,
622 D., Roehl, C. M., Wennberg, P. O., Griffith, D. W. T., Deutscher, N. M., Warneke, T., Notholt, J., Robinson, J., Sherlock,
623 V., Connor, B., Rettinger, M., Sussmann, R., Ahonen, P., Heikkinen, P., Kyrö, E., Mendonca, J., Strong, K., Hase, F.,
624 Dohe, S., and Yokota, T.: Improvement of the retrieval algorithm for GOSAT SWIR XCO₂ and XCH₄ and their validation
625 using TCCON data, *Atmospheric Measurement Techniques*, 6, 1533–1547, <https://doi.org/10.5194/amt-6-1533-2013>,
626 2013.

627 Zhang, L., Li, T., and Wu, J.: Deriving gapless CO₂ concentrations using a geographically weighted neural network:
628 China, 2014–2020, *International Journal of Applied Earth Observation and Geoinformation*, 114, 103063,
629 <https://doi.org/10.1016/j.jag.2022.103063>, 2022.

630 Zhang, M. and Liu, G.: Mapping contiguous XCO₂ by machine learning and analyzing the spatio-temporal variation in
631 China from 2003 to 2019, *Science of The Total Environment*, 858, 159588,
632 <https://doi.org/10.1016/j.scitotenv.2022.159588>, 2023.

633 Zhou, S., Wang, Y., Yuan, Q., Yue, L., and Zhang, L.: Spatiotemporal estimation of 6-hour high-resolution precipitation
634 across China based on Himawari-8 using a stacking ensemble machine learning model, *Journal of Hydrology*, 609,
635 127718, 2022.

636